

Lipid bilayer array for simultaneous recording of ion channel activities

Ayumi Hirano-Iwata,^{1,2,a)} Tomohiro Nasu,¹ Azusa Oshima,¹ Yasuo Kimura,³ and Michio Niwano^{1,3}¹Graduate School of Biomedical Engineering, Tohoku University, 6-6 Aoba, Aramaki, Aoba-ku, Sendai, Miyagi 980-8579, Japan²PRESTO, Japan Science and Technology Agency (JST), 4-1-8 Honcho Kawaguchi, Saitama 332-0012, Japan³Laboratory for Nanoelectronics and Spintronics, Research Institute of Electrical Communication, Tohoku University, 2-1-1 Katahira, Aoba-ku, Sendai, Miyagi 980-8577, Japan

(Received 23 April 2012; accepted 25 June 2012; published online 12 July 2012)

This paper describes an array of stable and reduced-solvent bilayer lipid membranes (BLMs) formed in microfabricated silicon chips. BLMs were first vertically formed simultaneously and then turned 90° in order to realize a horizontal BLM array. Since the present BLMs are mechanically stable and robust, the BLMs survive this relatively tough process. Typically, a ~60% yield in simultaneous BLM formation over 9 sites was obtained. Parallel recordings of gramicidin channel activities from different BLMs were demonstrated. The present system has great potential as a platform of BLM-based high throughput drug screening for ion channel proteins. © 2012 American Institute of Physics. [http://dx.doi.org/10.1063/1.4736263]

Ion-channel proteins regulate the ion flow across cell membranes¹ and are major targets for drug design.² Recording ion-channel currents is central to the investigation of the channel function as well as to drug screening applications. Development of high-throughput recording systems for ion-channel proteins is of great importance to improve the experimental efficiency. Several platforms that are capable of simultaneous recordings of ion-channel currents have been proposed, including patch-clamp arrays³ and bilayer lipid membrane (BLM) arrays.⁴⁻⁷ Although the patch-clamp method is a golden standard, reconstitution of ion channels in BLMs has an advantage that the researcher can precisely control the composition of the lipid environment, which is not easily manipulated with the patch-clamp method.

Several techniques have been reported as a platform for BLM arrays, such as microfluidic arrays^{3,5} and droplet interface bilayer arrays.⁷ Each platform offers advantages and disadvantages: for instance, microfluidic arrays allow for easy formation of multiple BLMs, but high surface to volume ratio of the microfluidic systems may be prone to false-negative due to adsorption of test drugs to the walls of microchannels.^{8,9} In addition, these approaches are commonly based on BLMs prepared from lipid solutions in unvolatile organic solvents, which are often criticized that some amount of the solvent remains in the central hydrophobic area of the BLMs¹⁰ and likely denatures ion-channel functions. For example, reconstitution of *N*-methyl-D-aspartate receptor channel in droplet interface bilayers¹¹ resulted in smaller single channel conductance than that reported for solvent-free bilayers¹² in a similar solution condition. In addition, Montal *et al.* recorded activities of acetylcholine receptor channels when they avoided the use of organic solvents.¹³ It is desirable to minimize organic solvent in membranes, though reduction of organic solvent may cause less stable BLMs than solvent-containing BLMs.¹⁴

The instability of the membranes is the main drawback of BLMs. While various microfabricated devices have been devoted to stabilize bilayers,¹⁵ these devices do not show increased stability except for prolonged lifetimes. Recently, we have reported on mechanically stable BLMs with minimized amount of solvent through the combination of silicon (Si) microfabrication and BLM formation.¹⁶ The BLMs showed tolerance to high applied voltage (± 1 V) and mechanical shocks during repetitive solution exchanges, together with long lifetime over 40 h. The key feature that stabilized BLMs is a tapered shape of the aperture edge with a nanometer-scale smoothness, which allows reduction of the stress on the bilayer at the contact with the chip, leading to stable BLMs without using large amount of solvents. In the present study, we have extended this stable BLM device to a 9-site horizontal array format. Simultaneous recording of channel current activities from the multiple BLMs was demonstrated by using a peptidic channel gramicidin. Such BLM array system could find wide-spread applications including drug discovery and development of sophisticated biosensors.

Microapertures with a diameter of 20–60 μm were fabricated in Si chips according to the procedure described in Ref. 16. The fabricated Si chip was silanized by treating with 2% (v/v) cyanopropyltrimethylchlorosilane (CPDS) in acetonitrile. BLMs were prepared by the monolayer folding method (Fig. 1).¹⁷ Nine Si chips were set in the middle of a Teflon chamber (Fig. 2). The system was assembled by stacking the bottom component, the Si chips, a perfluoroalkoxy polymer (PFA) sheet, and the top component. Both sides of the chips were pre-coated with *n*-hexadecane by dropping a 10- μl aliquot of 0.5% *n*-hexadecane in chloroform. A ~13-ml portion of 2.0 M KCl solution containing 10 mM HEPES/KOH (*pH* 7.4) was added to each compartment of the chamber. The water level in both compartments was set below the lowest apertures. A 75–100- μl portion of a lipid solution (7 mg/ml L- α -phosphatidylcholine (PC): L- α -phosphatidylethanolamine (PE): cholesterol = 7:1:2 (w/w) dissolved in chloroform/*n*-hexane (1:1, v/v)) was spread on

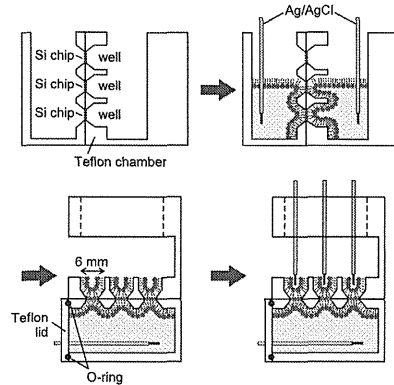


FIG. 1. Procedures for simultaneous BLM formation and rearrangement of the BLMs into a horizontal array format.

the aqueous solutions. After evaporation of the solvent, the water level was gradually raised over apertures to form BLMs at the flow rate of 10 ml/min using a KDS-260 syringe pump (KD Scientific). Incorporation of gramicidin channels into the BLMs was made by adding gramicidin A (Sigma) to the solutions in the both compartments and stirring for 1 h. Relatively, long stirring time was necessary to incorporate gramicidin, as it was more difficult to incorporate gramicidin into the present stable BLMs than into classical folded BLMs.¹⁸ Then, both Ag/AgCl electrodes were plugged off and the opening of the bottom component was covered with a Teflon lid (Fig. 1). A Perfluoro O-ring was used for sealing between the chamber and the lid. Then, the solution in the top component was discarded and the chamber was placed in order that the BLMs were aligned horizontally. Current recordings and capacitance measurements were performed with a sixteen-channel patch-clamp amplifier (Triton⁺, Tecella). The signal was low-pass filtered at 1 kHz, digitized at 10 kHz, and stored on-line. The data were analyzed using PCLAMP 10.2 software.

In the present system, all the BLMs were formed simultaneously and vertically by the folding method. The amount of an organic solvent required to form the BLMs is much less compared with the painting method,⁷ microfluidic systems,^{4,5} and droplet interface bilayers.^{6,11} This is a great advantage when we consider the application to drug screen-

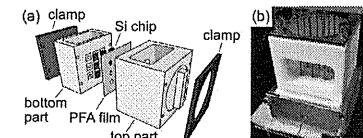


FIG. 2. (a) Drawing of the components of the present system, with the nine BLM sites placed in the Si chips. (b) Photograph of the experimental chamber in the final arrangement.

ings for ion-channel proteins, since fragile ion-channel proteins could hardly tolerate a direct exposure to an organic solvent.¹³ On the other hand, the vertical configuration of the BLMs is rather difficult to realize high throughput array systems. As horizontal formats are commonly used for microfluidic BLM arrays,^{4,5} a horizontal BLM array is more compatible with high throughput applications. We have designed an experimental setup, where the folded BLMs were first vertically formed and then turned 90° in order to realize a horizontal array of folded BLMs. The volume of each well was ~100 μl , which is suitable for solution handlings and minimizing potential problems associated with drug adsorption to the well surfaces.⁸

Fig. 1 shows our experimental protocol. After simultaneous formation of the BLMs, Ag/AgCl electrodes were plugged off and an aqueous solution in the top compartment was discarded. The BLMs were then laid horizontally and nine Ag/AgCl electrodes were inserted into respective wells. From four to seven BLMs were usually formed with the membrane resistance ranging from 1 to >100 G Ω . The overall probability of keeping BLMs in the horizontal array format, defined as the number of retained BLMs out of total well number examined (=9 \times trial number), was found to be 61% (60/99) out of 11 trials. Although we did not control possible pressure changes acting on the BLMs during sealing the bottom chamber with a Teflon lid (Fig. 1), which may cause BLM rupture, the observed yield is still higher than that (50%) reported for a microfluidic BLM array.⁴ Since the present BLMs were mechanically stable and robust, the BLMs survived such relatively tough process with a moderate yield. The BLMs in the horizontal array format withstood an applied voltage of ± 1 V, even when the applied potential was repeatedly switched (Fig. 3), demonstrating that the

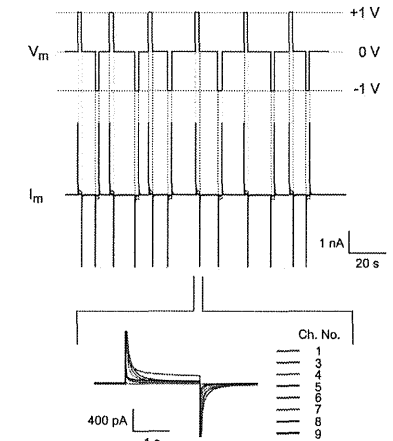


FIG. 3. An example of simultaneously recorded membrane currents (I_m) from eight BLMs when the applied potential (V_m) was repeatedly switched stepwise 0 V \rightarrow +1 V \rightarrow -1 V \rightarrow 0 V.

^{a)}Author to whom correspondence should be addressed. Electronic mail: ahirano@bme.tohoku.ac.jp. Present address: Graduate School of Biomedical Engineering, Tohoku University, 6-6 Aoba, Aramaki, Aoba-ku, Sendai, Miyagi 980-8579, Japan.

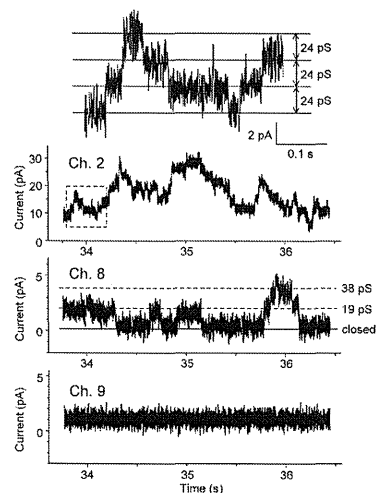


FIG. 4. Simultaneous current recording from three different BLMs. The box in the trace for Ch. 2 highlights the region shown in detail in the top trace.

arrayed BLMs still showed similar stability to those in the previous single BLM device.¹⁶ This voltage (± 1 V) is higher than the breakdown voltage (~ 300 – 400 mV) reported for BLMs prepared in plastic septa.^{19,20}

Fig. 4 shows an example of simultaneous current recordings from three BLMs with and without incorporated gramicidin channels. Gramicidin forms a channel that is permeable to monovalent cations, when gramicidin monomers form a membrane-spanning dimer. At the BLM formed in Ch. 8, distinct stepwise currents were seen with the single-channel conductance of ~ 19 pS. This level is similar to reported values (19–25 pS in 2.0 M KCl),^{16,21–23} confirming the functionality of the present BLMs. With a BLM containing multi channels (Ch. 2), much larger currents with multiple constant steps were observed. The conductance for each step was 24 pS, which is in agreement with gramicidin single-channel conductance. Since more channels were embedded in the BLM in Ch. 2, more frequent open \leftrightarrow close transitions were observed with shorter dwell time for each conductance level. No detectable current change was observed for Ch. 9, where no channel was incorporated into the BLM, demonstrating that no interference or crosstalk was detectable among simultaneously recorded BLMs.

In summary, we have succeeded in parallel formation of stable BLMs with minimized amount of solvents in a horizontal array format. All the BLMs were formed simultaneously by the folding method and then rotated 90° to be aligned horizontally. The yield of BLMs in the horizontal array is currently $\sim 60\%$, but this could be significantly

improved by optimizing the rotation process; the water level in the bottom compartment before placing the lid could be more accurately controlled by using automated injection, which will minimize the possible pressure change acting on the BLMs. Simultaneous recording of gramicidin channel activities demonstrates great potential of the present system as a platform of BLM-based high throughput drug screening systems. Although the present study used a 9-site array in order to provide a proof of principle for horizontal array of folded BLMs, in future work, we aim to improve the throughput by increasing the number of BLMs after changing the upper compartment to a detachable one. Combination with automation will also improve the experimental throughput. As the most critical folding process was already automated by using a syringe pump in the present study, we believe that our system can be fully automated including bilayer formation and current recordings.

This work was supported by Grant-in-Aids from Japan Society for the Promotion of Science (Grant Nos. 21350038 and 24350032) and JST (PRESTO). Finally, one (A.O.) of the authors thank the Japan Society for the Promotion of Science for research fellowships.

- ¹C. Miller, *Ion Channel Reconstitution* (Plenum, New York, 1986).
- ²J. P. Overington, B. Al-Lazikani, and A. L. Hopkins, *Nat. Rev. Drug Discovery* 5, 993 (2006).
- ³C. Py, M. Martina, G. A. Diaz-Quijada, C. C. Luk, D. Martinez, M. W. Denhoff, A. Charrier, T. Comas, R. Monette, A. Krantis, N. I. Syed, and G. A. R. Mealing, *Front. Pharmacol.* 2, 1 (2011).
- ⁴M. Zagnoni, M. E. Sandison, and H. Morgan, *Biosens. Bioelectron.* 24, 1235 (2009).
- ⁵B. Le Pionfle, H. Suzuki, K. V. Tsbata, H. Noji, and S. Takeuchi, *Anal. Chem.* 80, 328 (2008).
- ⁶R. Syeda, M. A. Holden, W. L. Hwang, and H. Bayley, *J. Am. Chem. Soc.* 130, 15543 (2008).
- ⁷G. Baaken, M. Sondermann, C. Schlemmer, J. Rühle, and J. C. Behrends, *Lab Chip* 8, 938 (2008).
- ⁸J. Dunlop, M. Bowlyby, R. Peri, D. Vasilyev, and R. Arias, *Nat. Rev. Drug Discovery* 7, 358 (2008).
- ⁹L. Guo and H. Guthrie, *J. Pharmacol. Toxicol. Methods* 52, 123 (2005).
- ¹⁰R. Benz, O. Fröhlich, F. Läger, and M. Montal, *Biochim. Biophys. Acta* 394, 323 (1975).
- ¹¹S. Leptihn, J. R. Thompson, J. C. Ellory, S. J. Tucker, and M. I. Wallace, *J. Am. Chem. Soc.* 133, 9370 (2011).
- ¹²A. Kloda, L. Lua, R. Hall, D. J. Adams, and B. Martinac, *Proc. Natl. Acad. Sci. U.S.A.* 104, 1540 (2007).
- ¹³N. Nelson, R. Anholt, J. Lindstrom, and M. Montal, *Proc. Natl. Acad. Sci. U.S.A.* 77, 3057 (1980).
- ¹⁴O. V. Batishchev and A. V. Indenbom, *Bioelectrochemistry* 74, 22 (2008).
- ¹⁵A. Hirano-Iwata, M. Niwano, and M. Sugawara, *Trends Anal. Chem.* 27, 512 (2008).
- ¹⁶A. Hirano-Iwata, K. Aoto, A. Oshima, T. Taira, R. Yamaguchi, Y. Kimura, and M. Niwano, *Langmuir* 26, 1949 (2010).
- ¹⁷M. Montal and P. Mueller, *Proc. Natl. Acad. Sci. U.S.A.* 69, 3561 (1972).
- ¹⁸A. Oshima, A. Hirano-Iwata, T. Nasu, Y. Kimura, and M. Niwano, *Micro Nanosyst.* 4, 2 (2012).
- ¹⁹M. Mayer, J. K. Kriebel, M. T. Tosteson, and G. M. Whitesides, *Biophys. J.* 85, 2684 (2003).
- ²⁰M. C. Peterman, J. M. Ziebarth, O. Braha, H. Bayley, H. A. Fishman, and D. M. Bloom, *Biomed. Microdev.* 4, 231 (2002).
- ²¹O. S. Andersen, *Biophys. J.* 41, 119 (1983).
- ²²D. D. Busath, C. D. Thulin, K. W. Hendershot, L. R. Phillips, P. Maughan, C. D. Cole, N. C. Bingham, S. Morrison, L. C. Baird, R. J. Hendershot, M. Cotten, and T. A. Cross, *Biophys. J.* 75, 2830 (1998).
- ²³A. Hirano-Iwata, T. Taira, A. Oshima, Y. Kimura, and M. Niwano, *Appl. Phys. Lett.* 96, 213706 (2010).

1.1 節 深部がん血管内治療用セラミック微小球

深部がん血管内治療用セラミック微小球

東北大学 川下 将一
 広西大学 李 志霞

1 はじめに

がんの最も一般的な治療法は、手術により患部を取り去る外科療法である。しかし、手術により切除した患部の機能が回復しない場合や、手術困難な場所にがんが発生する場合も多い。そこで近年、患部を切除しない、機能温存療法への期待が高まっている。患部を切除しない治療法としては、化学療法、放射線療法、免疫療法、温熱療法が挙げられる。しかし、体内深部のがんを効果的に治療する方法は十分には発達していない。

直径20～30 μm のある種のセラミック微小球は、図1に示すように、カテーテルによりがんのごく近傍の毛細血管に導入され、そこからがんを局所的に放射線(β 線)照射あるいは加温して治療しうる。同微小球は毛細血管を塞ぐので、がんへの栄養供給を断つ効果(塞栓効果)もあわせ示す。本稿では、そのような深部がんの血管内治療に貢献するセラミック微小球を紹介する。

2 血管内放射線治療用セラミック微小球

従来の放射線療法においては、体外から放射線を

照射するので、体内深部のがんに対して十分な量の放射線を照射しにくく、体表付近の正常細胞を傷めてしまう。最近では、ピンポイント放射線治療を旨とした定位放射線治療装置が臨床応用されているが、同装置においても、体外から放射線を照射するので、原理上、体表付近の照射ダメージを皆無にできない。また、放射性物質を封入した数mm程度の大きさの金属製カプセルを患部に埋入する方法が前立腺がんや舌がんなどの治療のために用いられているが、同法は進行がんにはあまり有効でなく、肝がんなどの体内深部に生じたがんへの適応は難しい。

2.1 イットリウム含有ガラス微小球

深部がん血管内放射線治療用微小球として最初に提案されたのは、 $17\text{Y}_2\text{O}_3-19\text{Al}_2\text{O}_3-64\text{SiO}_2$ (mol%) 組成のガラス微小球(YASガラス微小球)である¹⁾。同ガラス微小球は、ガラス粉末を混合ガス炎中に通して溶融し、表面張力により球状にした後、ふるい分けして得られる²⁾。このガラス微小球に中性子線を照射すると、ガラス中の ^{89}Y が ^{90}Y に変化し、半減期約64時間の β 線放射体となる³⁾。

このガラス微小球を肝動脈に挿入したカテーテルより肝がん患部に注入すると、その大部分が肝がんの細動脈内にとどまり、がんを局所的に直接放射線

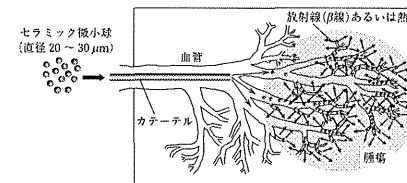


図1 セラミック微小球を用いた深部がん血管内放射線治療

照射する。同ガラスは優れた化学的耐久性を示す⁹⁾ので、治療中に放射性⁹⁰Yがガラスから溶出して他の正常組織を放射線照射する恐れはなく、治療後に微小球が体内に残存しても問題とならない⁹⁾。この放射性ガラス微小球による治療は外科手術を伴わないので、米国では治療を受けた患者は入院することなく、その日のうちに帰宅できる。このガラス微小球(TheraSphere[®]: MDS Nordion社, カナダ)は、世界各国において、手術不可能な部位に発生した肝がんの治療に用いられている⁹⁾。

2.2 酸化イットリウム微小球

YASガラス微小球は深部がんの血管内放射線治療を実現した点で画期的であるが、ガラス中に含まれるY₂O₃は17 mol%にすぎない。もし多量のイットリウムを含む微小球が得られれば、従来と同等の熱中性子線照射によって従来よりも高い放射能を微小球に付与できる、あるいは従来よりも短時間で治療に必要な放射能を微小球に与えることができる。高純度Y₂O₃粉末を原料とした高周波誘導熱プラズマ溶融法によれば、図2に示すような、直径20~30 μmのY₂O₃微小球が得られる⁷⁾。同微小球は体液環境下で優れた化学的耐久性を示す。また、131~173 MBqの放射性Y₂O₃微小球(15~30 mg)を、VX2腫瘍を埋植後2週間経過したウサギの肝臓に注入すると、図3に示すように、腫瘍増殖が顕著に抑制されることが確認されている⁸⁾。

最近では、表面が緻密で内部がハニカム状のY₂O₃微小球⁹⁾、中空Y₂O₃微小球¹⁰⁾、あるいは多孔性Y₂O₃マイクロ粒子¹¹⁾も提案されている。これらは、高周波誘導熱プラズマ溶融法により作製されたY₂O₃微小球よりも低いかさ比重を示すので、微小

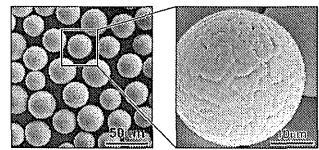


図2 高周波誘導熱プラズマ溶融法により作製したY₂O₃微小球の走査型電子顕微鏡写真⁷⁾

球注入の際に均一な懸濁液を得ることが容易であり、微小球注入時に患者の背側の血管に微小球が溜まる恐れもない。また、空孔内に薬剤を担持させることができれば、微小球に薬剤徐放能(DDS機能)を付与できる可能性がある。

2.3 リン酸イットリウム微小球

リン(P)は中性子線照射によりβ線放射体の³²Pとなり、その半減期は⁹⁰Yのそれよりもやや長い約14日である。したがって、リンを多量に含む微小球は、イットリウム含有ガラス微小球よりもやや長い期間にわたって治療効果を示すと期待される。

高周波誘導熱プラズマ溶融法によれば、YPO₄とY₂O₃からなる、化学的耐久性に優れた微小球が得られる⁷⁾。しかし、同法により得られた微小球の表面は平滑ではなく、その形状も歪である。表面凹凸の著しい微小球あるいは歪な形状の微小球は、カテーテルによる注入の際、血管壁を傷つける、あるいは目的の部位にまで到達できない恐れがあるので、臨床上、好ましくない。最近では、イットリウムイオンとリン酸イオンを含むゼラチン水溶液を水相とし、植物性油を油相としたエマルション反応場を利用すれば、表面が平滑なYPO₄微小球が得られ、同微小球が体液環境下で優れた化学的耐久性を示すことが明らかにされている¹²⁾。

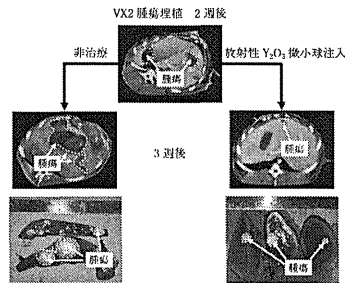


図3 放射性Y₂O₃微小球によるVX2腫瘍増殖抑制効果⁸⁾

3 温熱治療用セラミック微小球

腫瘍部は血流により冷却されにくく、加温されやすい。また、がん細胞は熱に弱く、43℃付近に加温されると死滅する。これに対し、正常細胞は約48℃まで損傷を受けない。したがって、がん患部を43℃付近に加温すると、がん細胞のみを死滅させることができる。このような、がん細胞が熱に弱い性質を利用した温熱療法が近年注目を集めている。しかし、体内深部に生じたがんを効果的に加温する手法は、まだ十分には発達していない。

磁力線は身体の深部にまで減衰することなく侵入しうる。マグネタイト(Fe₃O₄)やマグヘマイト(γ-Fe₂O₃)などの磁性体は交流磁場の下に置かれると発熱する。したがって、直径20~30 μmの磁性微小球を作製し、これをカテーテルにより深部がん

の近傍の毛細血管内に送り込み、その部位を交流磁場下に置くこと、がん患部を効果的に加温できる可能性がある。

3.1 マグネタイト微小球

直径約10 μmの市販のシリカ(SiO₂)ガラス微小球を、Fe₃O₄を飽和濃度含むフッ化水素酸水溶液中に浸漬し、さらにこれを還元性雰囲気中で加熱処理すると、図4(a)に示すような、直径25 μmのFe₃O₄微小球が得られる。同微小球は、約50 nmの大きさのFe₃O₄結晶からなり、飽和磁化53 emu·g⁻¹、保持力156 Oeの強磁性を示す。同微小球は、臨床応用可能な交流磁場条件(300 Oe, 100 kHz)の交流磁場の下において比較的良好な発熱特性を示す¹³⁾。最近では、図4(b)に示すような、酵素反応を用いて中空マグネタイト微小球を作製する試みも進められている¹⁴⁾。

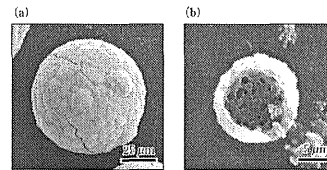


図4 Fe₃O₄微小球(a)¹³⁾および中空Fe₃O₄微小球の断面(b)¹⁴⁾の走査型電子顕微鏡写真

3.2 磁性ナノ粒子含有セラミック微小球

ゾルゲル法によれば、300 Oe, 100 kHzの交流磁場下で良好な発熱特性を示す磁性ナノ粒子(γ-Fe₂O₃・Fe₃O₄複合粒子、粒径約24 nm)¹⁵⁾を含有するシリカ(SiO₂)微小球が得られる(図5)¹⁶⁾。同微小球は、飽和磁化45.7 emu·g⁻¹、保持力43.9 Oeの強磁性を示し、図6に示すように、300 Oe, 100 kHzの交流磁場の下で良好な発熱特性を示す。上記手法によれば、磁性ナノ粒子を含むチタニア(TiO₂)微小球も作製できるが、磁性ナノ粒子の含有量はあまり多くない¹⁷⁾。今後、合成条件をさらに最適化し、磁性ナノ粒子の含有量を向上させる必要がある。

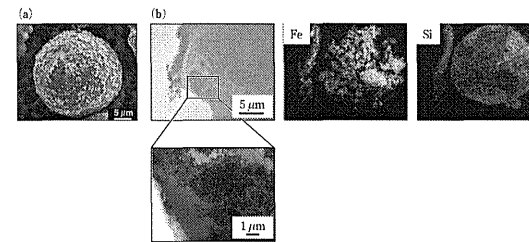


図5 (a)磁性ナノ粒子含有SiO₂微小球の走査型電子顕微鏡写真、(b)透過型電子顕微鏡写真および元素分布¹⁶⁾

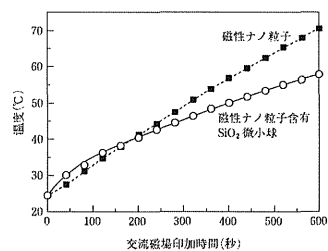


図6 25 mg · mL⁻¹ の濃度で寒天中に分散させた磁性ナノ粒子および磁性ナノ粒子含有 SiO₂ 微小球の 100 kHz, 300 Oe の交流磁場下における発熱特性¹⁵⁾

4 おわりに

本稿では深部がんの局所放射線あるいは温熱治療に役立つセラミック微小球を紹介した。セラミック微小球を用いた深部がん血管内治療法は、外科手術を伴わないので、治療時の患者の体力的および精神的負担を低減し、入院期間の短縮および患者の早期社会復帰を可能とする。したがって、同治療法は、がん患者数が著しく増加し、医師や病院ベッド数が不足する、いわゆる「がんの2015年問題」解決の一助にもなりうる。同治療法の1日も早い実現および普及が望まれる。

【引用・参考文献】

1) M.J. Hyatt and D.E. Day : *J. Am. Ceram. Soc.*, **70**, C283 (1987).

2) D.E. Day and T.E. Day : *An Introduction to Bioceramics*, pp.305-317, World Scientific, Singapore (1993).
 3) G.J. Ehrhardt and D.E. Day : *Nucl. Med. Biol.*, **14**, 233 (1987).
 4) E.M. Erbe and D.E. Day : *J. Biomed. Mat. Res.*, **27**, 1301 (1993).
 5) J.C. Andrews, S.C. Walker, R.J. Ackermann, L.A. Cotton, W.D. Ensminger and B. Shapiro : *J. Nucl. Med.*, **35**, 1637 (1994).
 6) <http://www.nordion.com/therasphere/>
 7) M. Kawashita, R. Shinya, H.-M. Kim, T. Kokubo, Y. Inoue, N. Araki, Y. Nagata, M. Hiraoka and Y. Sawada : *Biomaterials*, **24**, 2955 (2003).
 8) M. Kawashita : *Int. J. Appl. Ceram. Tech.*, **2**, 173 (2005).
 9) M. Kawashita, Y. Takayama, T. Kokubo, G.H. Takaoka, N. Araki and M. Hiraoka : *J. Am. Ceram. Soc.*, **89**, 1347 (2006).
 10) T. Miyazaki, T. Kai, E. Ishida, M. Kawashita and M. Hiraoka : *J. Ceram. Soc. Japan*, **118**, 479-482 (2010).
 11) M. Kawashita, N. Matsui, Z. Li and T. Miyazaki : *J. Mater. Sci. : Mater. Med.*, **21**, 1837-1843 (2010).
 12) M. Kawashita, N. Matsui, Z. Li, T. Miyazaki and H. Kanetaka : *J. Biomed. Mater. Res. Part B : Appl. Biomater.*, **99B**, 45-50 (2011).
 13) M. Kawashita, M. Tanaka, T. Kokubo, Y. Inoue, T. Yao, S. Hamada and T. Shinjo : *Biomaterials*, **26**, 2231 (2005).
 14) J. Zhao, H. Sekikawa, T. Kawai and H. Umuma : *J. Ceram. Soc. Japan*, **117**, 344 (2009).
 15) Z. Li, M. Kawashita, N. Araki, M. Mitsumori, M. Hiraoka and M. Doi : *Mater. Sci. Engin. C*, **30**, 990 (2010).
 16) Z. Li, M. Kawashita, N. Araki, M. Mitsumori, M. Hiraoka and M. Doi : *Biomed. Mater.*, **5**, 065010 (2010).
 17) Z. Li, M. Kawashita and M. Doi : *J. Ceram. Soc. Japan*, **118**, 467 (2010).

<川下 将一/李 志霞>

Enhancement of the Structural Stability of Full-Length Clostridial Collagenase by Calcium Ions

Naomi Ohbayashi, Noriko Yamagata, Masafumi Goto, Kimiko Watanabe, Youhei Yamagata and Kazutaka Murayama

Appl. Environ. Microbiol. 2012, 78(16):5839. DOI: 10.1128/AEM.00808-12.

Published Ahead of Print 8 June 2012.

Updated information and services can be found at:
<http://aem.asm.org/content/78/16/5839>

These include:

REFERENCES

This article cites 30 articles, 6 of which can be accessed free at:
<http://aem.asm.org/content/78/16/5839#ref-list-1>

CONTENT ALERTS

Receive: RSS Feeds, eTOCs, free email alerts (when new articles cite this article), [more»](#)

Information about commercial reprint orders: <http://journals.asm.org/site/misc/reprints.xhtml>
To subscribe to another ASM Journal go to: <http://journals.asm.org/site/subscriptions/>

Journals.ASM.org



Enhancement of the Structural Stability of Full-Length Clostridial Collagenase by Calcium Ions

Naomi Ohbayashi,^{1,a,b} Noriko Yamagata,² Masafumi Goto,^{3,*} Kimiko Watanabe,⁴ Youhei Yamagata,^{5,**} and Kazutaka Murayama⁶

¹Faculty of Pharmacy, Iwaki Meisei University, Fukushima, Japan; ²Graduate School of Biomedical Engineering, Tohoku University, Sendai, Japan; ³Graduate School of Agricultural Science, Tokyo University of Agriculture and Technology, Fuchu, Japan; ⁴Faculty of Medicine, Tohoku University, Sendai, Japan; ⁵and ⁶New Industry Creation Hatchery Center, Tohoku University, Sendai, Japan*

The clostridial collagenases G and H are multidomain proteins. For collagen digestion, the domain arrangement is likely to play an important role in collagen binding and hydrolysis. In this study, the full-length collagenase H protein from *Clostridium histolyticum* was expressed in *Escherichia coli* and purified. The N-terminal amino acid of the purified protein was Ala31. The expressed protein showed enzymatic activity against azocoll as a substrate. To investigate the role of Ca²⁺ in providing structural stability to the full-length collagenase H, biophysical measurements were conducted using the recombinant protein. Size exclusion chromatography revealed that the Ca²⁺ chelation by EGTA induced interdomain conformational changes. Dynamic light scattering measurements showed an increase in the percent polydispersity as the Ca²⁺ was chelated, suggesting an increase in protein flexibility. In addition to these conformational changes, differential scanning fluorimetry measurements revealed that the thermostability was decreased by Ca²⁺ chelation, in comparison with the thermal melting point (*T_m*). The melting point changed from 54 to 49°C by the Ca²⁺ chelation, and it was restored to 54°C by the addition of excess Ca²⁺. These results indicated that the interdomain flexibility and the domain arrangement of full-length collagenase H are reversibly regulated by Ca²⁺.

Collagens are an important component of animal tissues, which are composed of many different cell types. Collagenases specifically break down collagen, which has a tight triple helical structure and is resistant to most proteases. *Clostridium histolyticum* collagenases G and H (ColG and ColH) can easily digest collagens, regardless of their types and sizes (27). Therefore, they are used extensively as a clinical tool in the nonsurgical treatment of Dupuytren's disease (1, 13) and in the isolation of cells from tissues and organs, such as in the preparation of pancreatic islet cells for transplantation (5, 6, 15).

ColG and ColH require the presence of Ca²⁺ for their collagenolytic activity (2–4). The putative cleavage sites of ColG and ColH are the end portions and central portion of collagen, respectively (12, 20). The different cleavage sites may arise from the distinct domain architectures, that is, the different numbers of collagen binding domains (CBD) and polycystic kidney disease-like (PKD-like) domains. ColG and ColH consist of a collagenase module containing two domains, one or two copies of PKD-like domain, and one or two copies of CBD. A schematic diagram of the domain architectures of ColG and ColH is shown in Fig. 1. The percent sequence identity between these collagenases, calculated by ClustalW (26), is 41% for the entire sequences. The identities compared among individual domain types are 48% for the collagenase modules, 40 to 50% for the PKD-like domains, and 29 to 34% for the CBDs. The sequential alignments for the individual domains are shown in Fig. 2.

Structure determinations have been performed for the individual domains over the past few years. The crystal structures of the CBDs were solved as the apo- and holo-forms for ColG (29) and the holo-form for ColH (Protein Data Bank [PDB] entries 3JQX and 3JQW). The CBD structures revealed that two Ca²⁺ ions bind to the N-terminal linker region of the CBD and provide conformational stability to the CBD. Ca²⁺ binding is considered to have a critical role in enhancing interactions with collagen (29). Fur-

thermore, the collagen triple-helix binding mode was proposed by a nuclear magnetic resonance titration and small-angle X-ray scattering study (22). Recently, the structures of the collagenase module and PKD-like domain of ColG have been reported (9, 10). The collagenase module adopted a unique architecture, and a collagenolysis mechanism was proposed based on the structural information for the individual domains of ColG. In the PKD-like domain, Ca²⁺ was expected to bind to the N-terminal region of the domain as well as the CBD (9).

The cloning of the *colG* and *colH* genes facilitated the development of collagenase expression systems. The *Bacillus subtilis* expression system produced ColH as the secreted form, but the transformation efficiency was low (17). The *C. perfringens* expression system alleviated the translational problems and expressed ColH as the secreted form (25). The *Escherichia coli* expression system by Ducka et al. provided the effective production of the mature and various truncated forms of ColG, ColH, and ColT (from *Clostridium tetani*) (8).

Rapid progress has been made in clarifying the molecular mechanisms of the individual domains for both the function and structure. However, no structural studies of the entire collagenase molecule, as a multidomain protein, have been performed. Understanding the interplay of the domains is important, and structural information about the full-length protein should provide valuable insight about its function. Here, we report the biophysi-

Received 13 March 2012 Accepted 5 June 2012

Published ahead of print 8 June 2012

Address correspondence to Youhei Yamagata, y.yama@cc.iuat.ac.jp, or

Kazutaka Murayama, kmura@bme.tohoku.ac.jp.

Copyright © 2012, American Society for Microbiology. All Rights Reserved.

doi:10.1128/AEM.00808-12

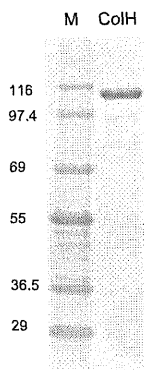


FIG 3 SDS-PAGE of purified ColH (0.8 μ g). M, molecular mass markers.

apparent molecular mass of 82 kDa is significantly smaller than expected.

The hydrodynamic radius was measured in the presence and the absence of EGTA by dynamic light scattering (DLS). The estimated molecular masses and the percent polydispersity were 108 kDa and 31.6% (without EGTA) and 116 kDa and 38.4% (with EGTA), respectively (Table 1). These results showed that ColH exists as a monomer in solution and that the particle size distribution increases by the addition of EGTA.

We further investigated the structural conservation of ColH by far-UV CD measurements in the presence and absence of 2 mM EGTA. The two CD spectra were essentially identical. Thus, the

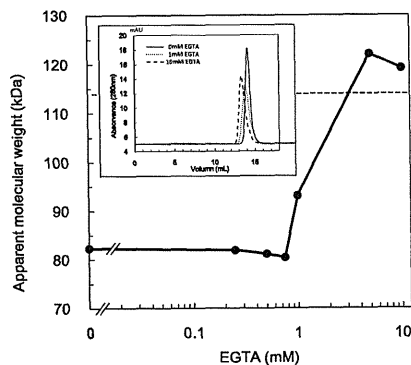


FIG 4 Size exclusion chromatography analysis of ColH with various concentrations of EGTA. The inset shows the size chromatography. The dashed line indicates the theoretical molecular mass of ColH (114 kDa).

TABLE 1 Hydrodynamic radius, estimated molecular mass, and percent polydispersity

EGTA	Hydrodynamic radius (nm)	Molecular mass (kDa)	% Polydispersity
-	4.40 (± 0.02)	108	31.6
+	4.54 (± 0.04)	116	38.4

secondary-structure elements and their arrangement in ColH were basically maintained in the presence and absence of Ca^{2+} .

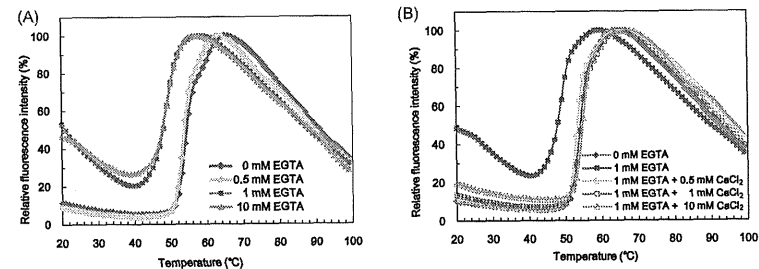
Enhancement of thermostability by calcium ions. Philominathan et al. showed that Ca^{2+} contributes to the thermostability of the CBD of ColG, by differential scanning calorimetry (DSC) (23). In this study, the thermostabilizing effect of Ca^{2+} toward ColH was measured by differential scanning fluorimetry (DSF) (11, 21, 28). Fluorescent dyes, including SYPRO orange and 1-anilino-naphthalene-8-sulfonic acid (ANS), bind to hydrophobic regions of proteins and show intense fluorescence. During the thermal unfolding process, hydrophobic regions of the protein are exposed to the solvent, resulting in the stimulation of dye binding and an increase in the fluorescence intensity.

The thermostability was evaluated from the change in the T_m (Fig. 5). The T_m of ColH with calcium was 54°C. In the presence of >1 mM EGTA, the T_m decreased to 49°C, suggesting destabilization. Subsequently, the protein solution was mixed with 1 mM EGTA before the DSF measurement, and then Ca^{2+} was added to the solution. As a result, the T_m was observed to recover from 49 to 54°C, as the Ca^{2+} concentration in the solution was increased. Hence, the addition of >1 mM Ca^{2+} led to the full recovery of the T_m . This result indicated that the presence of Ca^{2+} reversibly contributes to the thermostability of ColH.

As mentioned above, fluorescent dyes, such as SYPRO orange, are a useful tool to probe the existence of hydrophobic regions exposed to the solvent. In this study, a fluorescence analysis was conducted to assess the contribution of the hydrophobic interactions to the protein stability. Calmodulin, a known Ca^{2+} -binding protein, exposes its hydrophobic surfaces upon Ca^{2+} binding to stabilize protein-protein interactions (16, 18). We evaluated whether ColH also undergoes such a transition in the presence of Ca^{2+} . The fluorescence intensities of ColH were very weak at EGTA concentrations of less than 1 mM. However, the fluorescence intensity dramatically increased at EGTA concentrations of >1 mM (Fig. 6). These results indicated that hydrophobic regions of ColH are exposed by calcium chelation.

DISCUSSION

The structures of the CBDs have been solved for both ColG and ColH, and they harbor two calcium binding sites (29). The PKD-like domain structure has been reported for ColG (9). Although calcium binding was not observed in the crystal structure, a putative calcium binding site was proposed to exist near the N-terminal region of the domain. ColH contains a collagenase module (activator and peptidase domains), two PKD-like domains, and one CBD. Therefore, at least four calcium binding sites are expected to be present in this protein. All four binding sites are located near linker regions between domains. According to previous reports (4, 20), ColH can accept approximately five Ca^{2+} . It is possible that ColH has an additional Ca^{2+} binding site, perhaps in the linker regions for which structural data are missing.



EGTA (mM)	0	0.25	0.5	0.75	1	5	10
T_m (°C)	54	53	53	52	49	49	49

EGTA (mM)	0	1						
CaCl_2 (mM)	0	0	0.25	0.5	0.75	1	5	10
T_m (°C)	54	49	52	53	53	53	54	54

FIG 5 Thermal shift assay of ColH by differential scanning fluorimetry. (A) Effect of Ca^{2+} on the thermostability of ColH. (B) Recovery of the thermostability by the addition of CaCl_2 .

The size exclusion chromatography of full-length ColH revealed that the apparent molecular mass (82 kDa) was ~30% smaller than the calculated value (114 kDa). In the presence of EGTA (>1 mM), the apparent molecular mass was determined to be 119 kDa, which is comparable to the calculated value. The DLS measurements indicated that the percent polydispersity increased as EGTA was added, indicating an enhancement in the flexibility of the protein. No significant difference in the secondary structures was observed for the protein in the presence and absence of EGTA, according to the CD data. These results, therefore, suggest

that Ca^{2+} influences the interdomain conformation. The domain linker between the second PKD-like domain and CBD possesses two calcium binding sites (29). For the CBD of ColG, significant changes in the apparent molecular mass by Ca^{2+} chelation were observed in size exclusion chromatography and DLS (19, 29). However, no significant change in the hydrodynamic radius of ColH was observed in the DLS measurements. The conformational changes of ColH by calcium chelation may reduce the number of interactions with the matrix in the size exclusion chromatography column. Spectrometric measurements with the fluorescent dye indicated that hydrophobic interactions also contribute to the interdomain conformation of ColH. Remarkable conformational changes have been suggested for the N-terminal region of the CBD of ColG; however, the ANS fluorescence intensity in the presence and absence of Ca^{2+} did not change (23). Although the regions participating in the hydrophobic interactions have not been identified so far, they may be different from the linker region at the N terminus of the CBD.

Calcium ions were also found to influence the thermostability of full-length ColH. DSF measurements demonstrated that the T_m s decreased following calcium chelation. The difference in the T_m s was 5°C between the stabilized (with Ca^{2+} , 54°C) and destabilized (with EGTA, 49°C) states. The higher T_m was reversibly restored by the addition of excess Ca^{2+} . Among the domains in ColG and ColH, the thermostability of the second CBD of ColG was previously evaluated by DSC (23). The T_m s of the CBD apoferritin and a holo-form were determined to be 74 and 93°C, respectively. DSF and DSC are known to yield equivalent values as T_m estimations (14). Considering the sequence conservation between ColH and ColG, it can be assumed that the CBD of ColH also has relatively high T_m s. Consequently, the heat destabilization process in the initial stages of protein unfolding does not occur within the CBD of ColH. Although it is challenging to identify the initial region that is thermally destabilized, the peptidase domain and the following linker region are considered likely possibilities. The

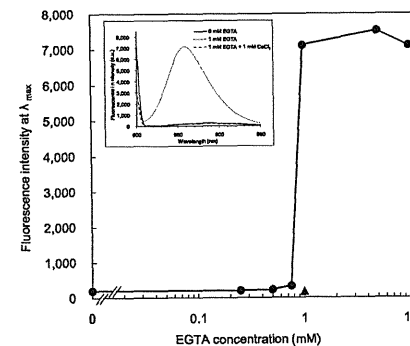


FIG 6 Fluorescence analyses of ColH with various concentrations of EGTA. The fluorescence intensity of ColH (2 μ M) was measured after the addition of EGTA (0 to 10 mM) (circles). The fluorescence intensity recovery point following the addition of 1 mM CaCl_2 is indicated by the triangle. The inset shows the fluorescence spectra of the sample solutions with 0 mM EGTA, 1 mM EGTA, and 1 mM EGTA plus 1 mM CaCl_2 .

structure of the PKD-like domain could not be exactly located in the crystal structure of ColG (Tyr119-Asn880) (10), and thus the collagenase module and the PKD-like domain may be flexibly linked.

In this study, we focused on full-length ColH as a multidomain structure and discussed the influence of interdomain flexibility on the arrangement of these individual domains. The results showed that the interdomain flexibility is predominantly and reversibly maintained by Ca^{2+} . The locations of the calcium binding sites are not known, except for the CBD. Nevertheless, the results presented herein indicate that the control of domain linker flexibility by Ca^{2+} plays an important structural role, and particular domain arrangement control mechanisms by Ca^{2+} may be commonly adopted by other collagenases, such as ColG.

ACKNOWLEDGMENTS

We acknowledge the support of the Biomedical Research Core of Tohoku University, Graduate School of Medicine. Part of this research was supported by the Coordination, Support and Training Program for Translational Research, from the Ministry of Education, Culture, Sports, Science and Technology, Japan.

REFERENCES

- Badalamente MA, Hurst LC. 2007. Efficacy and safety of injectable mixed collagenase subtypes in the treatment of Dupuytren's contracture. *J. Hand Surg. Am.* 32:767–774.
- Bond MD, Steinbrink DR, Van Wart HE. 1981. Identification of essential amino acid residues in Clostridium histolyticum collagenase using chemical modification reactions. *Biochem. Biophys. Res. Commun.* 102: 243–249.
- Bond MD, Van Wart HE. 1984. Characterization of the individual collagenases from Clostridium histolyticum. *Biochemistry* 23:3085–3091.
- Bond MD, Van Wart HE. 1984. Relationship between the individual collagenases of Clostridium histolyticum: evidence for evolution by gene duplication. *Biochemistry* 23:3092–3099.
- Brandhorst D, et al. 2005. Adjustment of the ratio between collagenase class II and I improves islet isolation outcome. *Transplant. Proc.* 37:3450–3451.
- Brandhorst H, et al. 2010. The effect of truncated collagenase class I isomers on human islet isolation outcome. *Transplantation* 90:334–335.
- Chavira R, Jr, Burnett TJ, Hageman JH. 1984. Assaying proteinases with azocoll. *Anal. Biochem.* 136:446–450.
- Ducka P, et al. 2009. A universal strategy for high-yield production of soluble and functional clostridial collagenases in *E. coli*. *Appl. Microbiol. Biotechnol.* 83:1055–1065.
- Eckhard U, Brandstetter H. 2011. Polycystic kidney disease-like domains of clostridial collagenases and their role in collagen recruitment. *Biol. Chem.* 392:1039–1045.
- Eckhard U, Schonauer E, Nuss D, Brandstetter H. 2011. Structure of collagenase G reveals a chew-and-digest mechanism of bacterial collagenolysis. *Nat. Struct. Mol. Biol.* 18:1109–1114.
- Ericsson UB, Hallberg BM, Delitta GT, Dekker N, Nordlund P. 2006. Thermofluor-based high-throughput stability optimization of proteins for structural studies. *Anal. Biochem.* 357:289–298.
- French MF, Mookhtiar KA, Van Wart HE. 1987. Limited proteolysis of type I collagen at hyperreactive sites by class I and II Clostridium histolyticum collagenases: complementary digestion patterns. *Biochemistry* 26:681–687.
- Gilpin D, et al. 2010. Injectable collagenase Clostridium histolyticum: a new nonsurgical treatment for Dupuytren's disease. *J. Hand Surg. Am.* 35:2027–2038.e1.
- He F, Hogan S, Latypov RF, Narhi LO, Razinkov VI. 2010. High throughput thermostability screening of monoclonal antibody formulations. *J. Pharm. Sci.* 99:1707–1720.
- Helley TJ, Stern PH, Brand JS. 1983. Enzymatic isolation of cells from neonatal calvaria using two purified enzymes from Clostridium histolyticum. *Exp. Cell Res.* 149:227–236.
- Ikura M. 1996. Calcium binding and conformational response in EF-hand proteins. *Trends Biochem. Sci.* 21:14–17.
- Jung CM, et al. 1999. Identification of metal ligands in the Clostridium histolyticum ColH collagenase. *J. Bacteriol.* 181:2816–2822.
- LaPorte DC, Wierman BM, Storm DR. 1980. Calcium-induced exposure of a hydrophobic surface on calmodulin. *Biochemistry* 19:3814–3819.
- Matsushita O, Koide T, Kobayashi R, Nagata K, Okabe A. 2001. Substrate recognition by the collagen-binding domain of Clostridium histolyticum class I collagenase. *J. Biol. Chem.* 276:8761–8770.
- Mookhtiar KA, Van Wart HE. 1992. Clostridium histolyticum collagenases: a new look at some old enzymes. *Matrix Suppl.* 1:116–126.
- Niesen FH, Berglund H, Vedadi M. 2007. The use of differential scanning fluorimetry to detect ligand interactions that promote protein stability. *Nat. Protoc.* 2:2212–2221.
- Philominathan ST, et al. 2009. Unidirectional binding of clostridial collagenase to triple helical substrates. *J. Biol. Chem.* 284:10866–10876.
- Philominathan ST, Matsushita O, Gensure R, Sakon J. 2009. Ca^{2+} -induced linker transformation leads to a compact and rigid collagen-binding domain of Clostridium histolyticum collagenase. *FEBS J.* 276: 3589–3601.
- Smith PK, et al. 1985. Measurement of protein using bicinchoninic acid. *Anal. Biochem.* 150:76–85.
- Tamai E, et al. 2008. High-level expression of his-tagged clostridial collagenase in Clostridium perfringens. *Appl. Microbiol. Biotechnol.* 80: 627–635.
- Thompson JD, Higgins DG, Gibson TJ. 1994. CLUSTAL W: improving the sensitivity of progressive multiple sequence alignment through sequence weighting, position-specific gap penalties and weight matrix choice. *Nucleic Acids Res.* 22:4673–4680.
- Toyoshima T, et al. 2001. Collagen-binding domain of a Clostridium histolyticum collagenase exhibits a broad substrate spectrum both in vitro and in vivo. *Connect. Tissue Res.* 42:281–290.
- Vedadi M, et al. 2006. Chemical screening methods to identify ligands that promote protein stability, protein crystallization, and structure determination. *Proc. Natl. Acad. Sci. U. S. A.* 103:15835–15840.
- Wilson JJ, Matsushita O, Okabe A, Sakon J. 2003. A bacterial collagen-binding domain with novel calcium-binding motif controls domain orientation. *EMBO J.* 22:1743–1752.
- Yoshihara K, Matsushita O, Minami J, Okabe A. 1994. Cloning and nucleotide sequence analysis of the colH gene from Clostridium histolyticum encoding a collagenase and a gelatinase. *J. Bacteriol.* 176:6489–6496.

Properties of *N*-Butyl Cyanoacrylate-iodized Oil Mixtures for Arterial Embolization: In Vitro and In Vivo Experiments

Chiaki Takasawa, MD, PhD, Kazumasa Seiji, MD, PhD,
Kenichi Matsunaga, MD, PhD, Toshio Matsuhashi, MD, PhD,
Makoto Ohta, PhD, Shuya Shida, Kei Takase, MD, PhD, and
Shoki Takahashi, MD, PhD

ABSTRACT

Purpose: To examine the properties of *N*-butyl cyanoacrylate (NBCA) and iodized oil (lipiodol [Lip]) in vitro and in vivo for safe and effective embolization.

Materials and Methods: Viscosity, polymerization time, and diffusing capacity were evaluated according to the NBCA/Lip ratio in vitro. Additionally, the effect of the NBCA/Lip ratio on arterial embolization was evaluated in vivo; various ratios of NBCA/Lip were injected into the renal arteries of adult beagles, after which the embolization effect following transcatheter arterial embolization was quantitatively investigated histopathologically and using computed tomography (CT) volumetry.

Results: The viscosity of NBCA/Lip increased, polymerization time was prolonged, and diffusing capacity increased as the NBCA density decreased. As the NBCA density decreased, embolic material was recognized in smaller diameter arteries, and embolization of a larger vascular bed was accomplished. The NBCA/Lip mixture with a low density of NBCA was located more peripherally from the catheter tip, and embolization of more peripheral and smaller diameter arteries was achieved.

Conclusions: The relationships of properties of NBCA/Lip in vitro and embolization effects in vivo of various ratios of NBCA/Lip were quantitatively examined and compared. The results of this study are useful for safe and effective embolization.

ABBREVIATIONS

Lip = lipiodol, NBCA = *N*-butyl cyanoacrylate

N-butyl cyanoacrylate (NBCA) (Histoacryl; B. Braun Melsungen AG, Melsungen, Germany) is a liquid, permanent embolic material used for transcatheter arterial embolization that polymerizes in the presence of anions. Because the embolization mechanism of NBCA does not depend on

clotting function, it still has a marked embolic effect when clotting function is impaired (1,2). For embolization, NBCA is mixed with iodized oil (Lipiodol [Lip]); Terumo, Tokyo, Japan) in a ratio between 1:1 and 1:9. This mixing is done for two reasons: (a) to produce a radiopaque material because NBCA is radiolucent and is not observed on fluoroscopy and (b) to adjust the time for polymerization from injection (polymerization time) and the time for completion of embolization by changing the density of NBCA; this allows the material to reach successfully, but not pass through, target blood vessels, possibly with an arteriovenous shunt.

Regarding the mixture ratio, there are two conflicting opinions. One opinion is that the lower the NBCA density, the more peripherally the embolic material reaches because the polymerization time is prolonged. Alternatively, it has been suggested that the lower the NBCA density, the more proximally the embolic material ceases to flow because the viscosity of NBCA/Lip is increased owing to a high Lip density. Clinically, the NBCA/Lip ratio is empirically de-

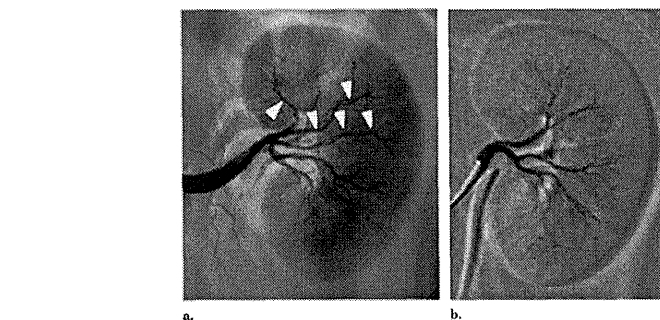


Figure 1. Digital subtraction angiogram of renal artery obtained before and after embolization. (a) Left renal artery angiogram obtained before embolization. (b) Left renal artery angiogram obtained after embolization with NBCA-Lip (1:1). The arteries indicated by arrowheads underwent embolization.

cided by a physician performing transcatheter arterial embolization after considering the blood vessel diameter and blood velocity. However, the exact relationship between the NBCA/Lip ratio and intravascular polymerization factors is unknown.

To study intravascular polymerization factors on the side of the embolic material, we evaluated the viscosity, diffusing capacity, and polymerization time of NBCA/Lip according to their ratio in vitro. Additionally, we examined the effect of the NBCA/Lip ratio on arterial embolization in vivo; various ratios of NBCA-Lip were injected into the renal arteries of adult beagles, after which the embolization effect was quantitatively investigated using computed tomography (CT) volumetry and histopathologically. Finally, we assessed how the polymerization time and viscosity of the NBCA/Lip ratio affected arterial embolization.

MATERIALS AND METHODS

This study was approved by the local animal experiment committee.

In Vitro Studies

Viscosity of NBCA/Lip Mixture. The viscosity of the NBCA/Lip mixture was determined using a tuning fork-type viscometer (SV-10; A&D Company, Tokyo, Japan). We measured the viscosity of samples at eight different NBCA/Lip ratios (NBCA:Lip = 1:1 [NBCA density 50%], 1:2 [33%], 1:3 [25%], 1:4 [20%], 1:5 [16.7%], 1:6 [14.3%], 1:7 [12.5%], 1:8 [11.1%], 1:9 [10%]) at a temperature of 37°C. We used Win CT-Viscosity software (A&D Company) to analyze the measurement results.

Diffusing Capacity of NBCA/Lip. When mixed with blood, NBCA/Lip is polymerized to generate a polymer.

The diffusing capacity of NBCA/Lip was evaluated by measuring the area of the generated polymer in blood after its mixing with blood. NBCA/Lip (0.5 mL) was dropped on whole blood (1 mL) from an adult beagle on a Petri dish and shaken with a shaker 100 times per minute. Next, the area of the polymer was measured using Scion image software (National Institutes of Health, Bethesda, Maryland).

Polymerization Time. To determine the polymerization time, NBCA/Lip was dropped on blood, and we recorded the state of polymerization by video (EXILJM EX-FH25; Casio, Tokyo, Japan) at a frame rate of 240 frames/s and observed the morphologic changes in the polymer. The completion of polymerization was defined as the time point when the morphologic changes ceased.

In Vivo Studies

Twelve adult beagles were used for the in vivo experiment (mean body weight, 14.9 kg; range, 13.8–15.8 kg). The dogs were anesthetized with an intramuscular injection of ketamine (40 mg/kg of body weight) and atropine sulfate (0.1 mg). Sodium pentobarbital (Nembutal, 25 mg/kg; Dainippon Sumitomo Pharma, Osaka, Japan) was used as a supplemental anesthetic.

Transcatheter Arterial Embolization. For transcatheter arterial embolization, an 8-F introducer sheath (Medikit, Tokyo, Japan) was inserted into the carotid artery. A baseline angiogram of the abdominal aorta was obtained using a 5-F Cobra catheter (Cook, Inc, Bloomington, Indiana), and then the renal artery was catheterized (Fig 1). A 2-F microcatheter (Renegade; Boston Scientific, Natick, Massachusetts) was placed coaxially through the 5-F catheter and positioned distally in the ventral or dorsal branch. Selective embolizations with NBCA/Lip were performed by the same radiologist.

From the Departments of Diagnostic Radiology (C.T., K.S., K.T., S.T.) and Institute of Fluid Science (M.O., S.S.), Tohoku University, 2-1-1 Katahira Aoba-ku Sendai, 980-8577, Japan, Takeda General Hospital (K.M.), Aizuwakamura, and JR Sendai Hospital (T.M.), Aoba-ku, Sendai, Japan. Received February 17, 2012; final revision received June 17, 2012; accepted June 20, 2012. Address correspondence to S.K.; E-mail: k-seiji@rad.med.tohoku.ac.jp

This material was presented at the SIR 2012 Annual Meeting.

Figures E1–E3 are available online at www.jvir.org.

None of the authors have identified a conflict of interest.

© SIR, 2012

J Vasc Interv Radiol 2012; 23:1215–1221

<http://dx.doi.org/10.1016/j.jvir.2012.06.022>

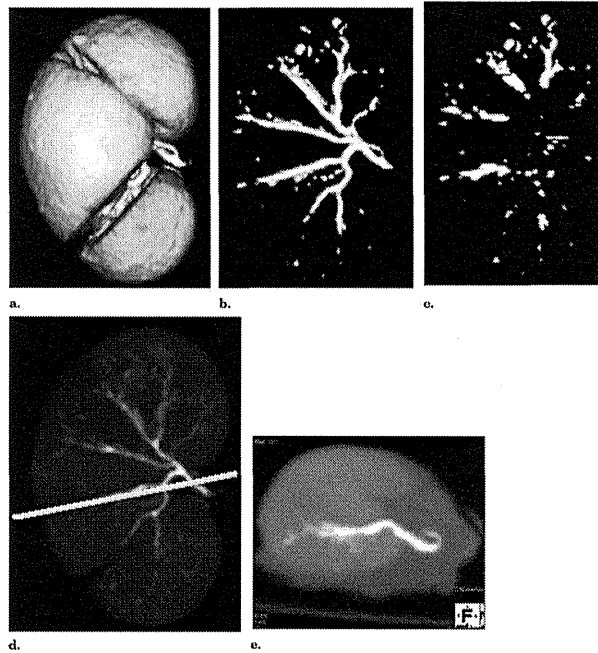


Figure 2. CT volume rendering image and volumetry of the kidney after embolization with NBCA-Lip (1:9). (a) CT volume rendering image of the kidney. (b) CT volume rendering image of the region with a CT value > 500 HU. CT volumetry of this region evaluates the total vascular bed in which the embolic material was distributed. (c) By removing the medullary vessels on source images, volumetry of the vascular bed in which embolization was accomplished only in the cortex was achieved. To consider individual differences in the vascular bed of the kidney, the cortex/total kidney ratio was evaluated. This was considered to be the index of the distal embolization effect. (d) Maximum intensity projection of the kidney. (e) CT axial image of the position of the line on image (d). For pathologic preparation, a region with a high level of NBCA-Lip on CT similar to this was chosen.

The embolization technique was performed as follows: NBCA was mixed with Lip at a ratio of 1:1, 1:3, or 1:9 manually. Before injecting NBCA/Lip, the microcatheter was flushed with 5% dextrose to prevent premature polymerization of the NBCA/Lip triggered by anions from residual blood or saline. NBCA/Lip was injected carefully under fluoroscopic monitoring using a 2.5-mL syringe. Injection speed was decided by the operator to prevent blood stasis. The endpoint of embolization was decided by the operator at the time of flow arrest of NBCA/Lip at fluoroscopy.

Immediately after injection, the microcatheter was retracted to prevent the catheter tip from adhering to the vessel wall. Next, the inner lumen of the guiding catheter was aspirated, and the contralateral embolization procedure was performed using a new microcatheter. The injected

volume was measured by subtracting microcatheter luminal volume (0.67 mL) from the injected volume. Embolization was performed in eight kidneys using each NBCA/Lip ratio.

CT Volumetry. Immediately after embolization, the dog was killed with an overdose of sodium pentobarbital; exsanguination was performed, and the kidneys were removed. A CT scan of the specimen was obtained, and the intravascular distribution of Lip was confirmed using 64-slice multidetector CT (Aquilion 64; Toshiba, Tokyo, Japan). Using CT volume-rendering images of the kidney with a threshold CT value > 500 HU, CT volumetry of the vascular bed after embolization was performed at a workstation (Ziostation version 1.3.0.2.; AMIN, Inc, Tokyo, Japan) (Fig 2). We measured the volume of cortical vessels

that underwent embolization after removing the medullary vessels on source images and evaluated the vascular bed in which embolization was achieved only in the periphery, not including the medullary part of the kidney. For the index of the distal embolization effect, we did not use the absolute value of the cortical vessels that underwent embolization but rather the ratio of vessels of the cortex that underwent embolization and those of the entire kidney (V-cortex/V-kidney) to exclude the variation effect of different volumes of the renovascular bed among different subjects.

Histopathologic Evaluation. The specimen was fixed in 10% neutral buffered formalin solution for 1 to 2 weeks and then was subjected to alcohol dehydration. Additionally, a region with a high level of NBCA/Lip on CT was chosen for pathologic preparation. This tissue was embedded in paraffin and stained with hematoxylin and eosin and Elastica-Masson. After a preliminary experiment of renal artery embolization with NBCA alone, NBCA/Lip, and Lip alone, embolic material was pathologically identified as amorphous structures that stained with either hematoxylin and eosin or Elastica-Masson within vessels that underwent embolization; these amorphous structures were never seen in control vessels that did not undergo embolization.

In each kidney, 40 random fields were observed at 400× magnification. A histopathologic evaluation determined the following two points to evaluate how far the NBCA/Lip traveled in the artery: (a) point 1, the smallest minor axis of the arteriole containing embolic material in the lumen was measured in each kidney; (b) point 2, the number of arterioles with a minor axis $\leq 40 \mu\text{m}$ containing embolic material in the lumen was counted. A sampling error secondary to specimen preparation may affect point 1, so point 2 was used as another index of the distal embolism effect, which could be regarded as quantitative evaluation of the distal embolism effect.

Statistical Analysis

Statistical analysis was performed using the SPSS software package (version 15.0; SPSS Inc, Chicago, Illinois). Histopathologic evaluations were compared using analysis of variance (ANOVA) with the Tukey-Kramer post hoc test. A *P* value < .05 was considered statistically significant.

RESULTS

In Vitro Studies

With the increased amount of Lip, both the viscosity of NBCA/Lip and the area of the polymer increased (Figs 3 and 4). The polymerization time also increased with the Lip volume (Fig 5).

In Vivo Studies

Transcatheter arterial embolization of the renal artery succeeded in all cases. On average, 0.43 mL (range, 0.3–0.6

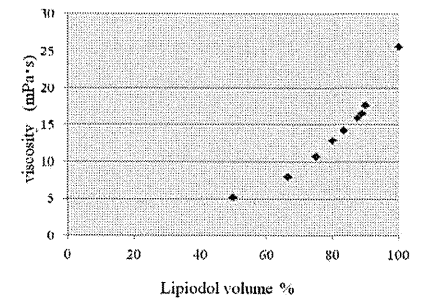


Figure 3. Viscosity of NBCA-Lip. The viscosity of NBCA-Lip increased exponentially with the volume of Lip.

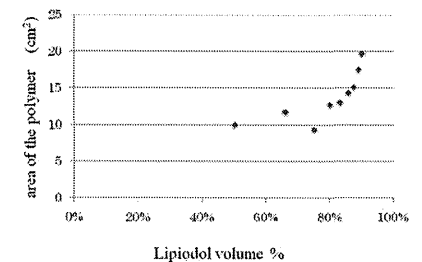


Figure 4. Diffusing capacity of NBCA-Lip. As an index of the diffusing capacity of the NBCA-Lip polymer in blood, we measured the area of the polymer on a Petri dish. The area of the polymer increased exponentially with the volume of Lip.

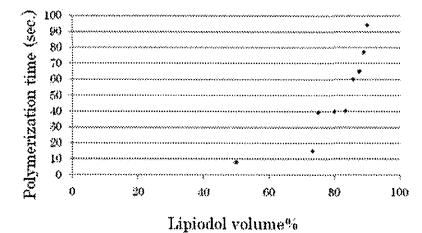


Figure 5. Polymerization time of NBCA-Lip. The polymerization time increased with the Lip volume. The time was similar between ratios 1:1 and 1:2 and between ratios 1:3 and 1:5 and increased exponentially in ratios 1:6–1:9.

mL) of NBCA/Lip was required to achieve embolization in all kidneys. No significant difference was noted in the quantity injected among the three groups.

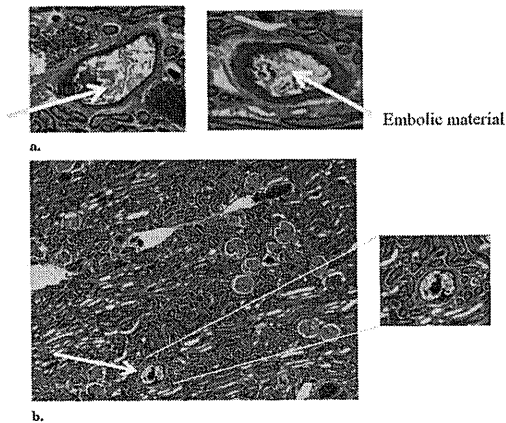


Figure 6. Photomicrograph of renal medulla obtained immediately after embolization with NBCA-Lip. (Elastica-Masson; original magnification, $\times 400$.) (a) Section of arteriole of renal medulla. The amorphous material in the artery is embolic material. (b) The smallest minor axis of the arteriole containing embolic material in the lumen was measured in each kidney.

The cortical vascular bed in which embolization was achieved increased as the Lip volume increased. The cortical vascular bed in which embolization was achieved was significantly greater with NBCA/Lip ratios of 1:3 and 1:9 than with NBCA/Lip ratio of 1:1; no significant difference was observed between NBCA/Lip ratios of 1:3 and 1:9 (Fig E1 [available online at www.jvir.org]).

Regarding evaluation point 1 (Fig 6 and Fig E2 [available online at www.jvir.org]), the minimum minor axis of an arteriole that contained embolic material in the lumen was 3.4 μm , 2.2 μm , and 2.3 μm with NBCA/Lip ratios of 1:1, 1:3, and 1:9. With ratios of 1:3 and 1:9, the embolic material was found in significantly narrower arterioles than with a ratio of 1:1.

Regarding evaluation point 2 (Fig E3 [available online at www.jvir.org]), the average number of arterioles in which embolization was accomplished in 40 fields was 1.1, 5.6, and 6.3 with ratios of 1:1, 1:3, and 1:9. At a low NBCA density, embolization was achieved in narrow arterioles, and the peripheral distribution of the embolic material tended to be wider. Embolization was achieved in more arterioles at a 1:9 ratio than at a 1:1 ratio; no significant difference was found between 1:1 and 1:3 ratios and between 1:3 and 1:9 ratios.

DISCUSSION

When performing transcatheter arterial embolization, reaching as close to the target as possible with embolization of only the target artery is critical. When embolization

occurs prematurely or much proximal to the target, only a temporary embolization effect may result because recanalization via collateral circulation would develop. Embolization immediately proximal to the target (ie, distal embolization) is needed to obtain a permanent embolization effect on the target. However, selective insertion of the microcatheter is often difficult because of increased tortuosity or small size of the target artery. When some distance consequently remains between the microcatheter tip and the target, distal embolization that would be desirable may become unachievable.

Little is known regarding the polymerization time of NBCA/Lip after injection, and a risk exists of excessive or incomplete embolization or adhesion of the catheter tip to the vascular wall. The ratio is empirically decided by an interventional radiologist considering the blood vessel diameter, blood velocity, and distance from the microcatheter tip to the target. Successful embolization has been reported at the following ratios for different target arteries: bronchial artery, 1:7 (3); gastrointestinal organs, 1:1–1:7; splenic artery, 1:3–1:4; lower dorsal branch of the renal artery, 1:4 (2); lumbar artery, 1:1; inferior epigastric artery, 1:7; and iliac artery, 1:5. However, the optimal ratio may not be constant for each artery and may differ in different cases depending on circumstances such as the blood vessel diameter, blood velocity, and distance from the microcatheter tip to the target.

Experimental examination of the embolization effect of NBCA has been reported. Performing embolization of rat renal arteries with different ratios of NBCA/Lip (1:1

and 1:4), Sadato et al (4) evaluated the histopathology at several time intervals after embolization. Their results showed no recanalization of the vessels in which embolization was achieved, although it was not disclosed how far distally the embolic material traveled. Other studies reported the relationship between the number of arteries in which embolization was achieved and the ischemic changes in the intestinal tract wall according to different ratios of NBCA/Lip (5,6). However, no study had quantified the relationship between the NBCA/Lip ratio and the degree of the embolic effect or how far distally the embolic material reached.

We conducted the present study to examine quantitatively the relationship of property in vitro (viscosity, diffusing capacity, and polymerization time) and embolization effect in vivo of various ratios of NBCA/Lip. In the in vitro study, which used a more modern and precise method with a high-speed camera, we confirmed more objectively that the polymerization time increased with the Lip volume, which was indicated in previous experimental studies using traditional methods (7–9). The difference in the polymerization time according to the differential ratio might have resulted because it occurred only where the NBCA/Lip came into contact with blood but not in the remaining part where it was separate from the blood. Lip could have inhibited the contact between NBCA and blood and polymerization. We presume that the actual polymerization time during transcatheter arterial embolization might be shorter than the results in our in vitro study because of more likely contact between NBCA/Lip and blood.

In the in vivo experiment with histopathologic measurement of number and axis of arterioles, embolization occurred more distally at a 1:3 ratio than at a 1:1 ratio. However, no significant difference was found between 1:3 and 1:9 ratios in vivo, where polymerization time and viscosity greatly changed in vitro. The exact reason for this finding is unclear, but there might have been some interaction of the peripheral arterial embolization effect with viscosity within an extremely narrowed lumen; increased viscosity owing to a high ratio of Lip may disproportionately reduce blood flow within small arterioles or capillaries, resulting in a relatively limited degree of peripheral embolization. This aspect was not investigated in our in vitro study. The kinetics of NBCA/Lip may be modified by not only polymerization time and viscosity but also other factors, including blood vessel diameter, blood velocity, and blood pressure and their combination, which remain to be evaluated.

Similar to histopathologic measurement, the cortical vascular bed that underwent embolization (not including the medullary part of the kidney) measured by CT volumetry was significantly greater with NBCA/Lip ratios of 1:3 and 1:9 than a ratio of 1:1, although quantity of NBCA/Lip injected was not significantly different among the three groups. This finding may indicate that the medullary (not cortical) vascular bed that underwent

embolization was greater at the mixture ratio of 1:1 than the ratios of 1:3 and 1:9.

It was presumed from the in vitro results on viscosity and diffusing capacity that NBCA/Lip likely flows more peripherally in blood vessels in vivo when the NBCA density is decreased. In our in vivo study, although no significant difference was found between 1:3 and 1:9 ratios, both the number of arteries in which embolization was achieved on pathologic examination (Fig E3 [available online at www.jvir.org]) and the vascular bed in which embolization was achieved on CT volumetry (Fig E1 [available online at www.jvir.org]) were larger with the ratio of 1:9 than with 1:3. These results may contradict the opinion that NBCA/Lip does not easily reach peripheral arteries when the Lip density is increased. Based on the in vitro results of polymerization time and in vivo results, we suggest using the ratio of less dense NBCA (closer to 1:9) when there remains some distance between the microcatheter tip and the target to avoid premature or too proximal embolization. Information acquired in this study on the relationship between the NBCA/Lip ratio and intravascular polymerization factors would help decide the ratio in individual cases in terms of safe and effective embolization.

The limitations of this study include our examinations only of NBCA/Lip ratios of 1:1–1:9, as these are frequently clinically used. We were able to determine the relationships of the viscosity, the polymerization time, and the embolism effect in this range. However, we did not confirm whether similar relationships are maintained with a different range of ratios.

In conclusion, we quantitatively examined the relationship of properties of NBCA/Lip in vitro and embolization effects in vivo of various ratios of NBCA/Lip and compared the data. The results of this study are useful for safe and effective embolization.

ACKNOWLEDGMENT

The authors acknowledge Yasuhiro Nakamura, Fumiyoshi Fujishima, Kazuhiro Sato, and Tomoyoshi Kimura.

REFERENCES

- Yonemitsu T, Kawai N, Sato M, et al. Evaluation of transcatheter arterial embolization with gelatin sponge particles, microcoils, and N-butyl cyanoacrylate for acute arterial bleeding in a coagulopathic condition. *J Vasc Interv Radiol* 2009; 20:1176–1187.
- Lee CW, Liu KL, Wang HF, Chen SJ, Tsang YM, Liu HM. Transcatheter arterial embolization of acute upper gastrointestinal tract bleeding with N-butyl-2-cyanoacrylate. *J Vasc Interv Radiol* 2007; 18:209–216.
- Feyyaz B, Nuri CC, Korkut B, Mustafa Y, Nihat K. Transarterial microcatheter glue embolization of the bronchial artery for life-threatening hemoptysis: technical and clinical results. *Eur J Radiol* 2010; 73:380–384.
- Sadato A, Wakhloo AK, Hopkins LN. Effects of a mixture of a low concentration of n-butylcyanoacrylate and ethiodol on tissue reactions and the permanence of arterial occlusion after embolization. *Neurosurgery* 2000; 47:1197–1205.

5. Ogawa Y, Takizawa K, Funakubo M, Yagihashi K, Nakajima Y, Tadokoro M. A histological study in an animal model after embolization of the mesenteric artery with N-butyl-2-cyanoacrylate. *J Abdom Emerg Med* 2008; 28:775-780.
 6. Jae HJ, Chung JW, Kim HC. Experimental study on acute ischemic small bowel changes induced by superselective embolization of superior mesenteric artery branches with N-butyl cyanoacrylate. *J Vasc Interv Radiol* 2008; 19:755-763.

7. Brothers MF, Kaufmann JC, Fox AJ, Deveikis JP. n-Butyl 2-cyanoacrylate—substitute for IBCA in interventional neuroradiology: histopathologic and polymerization time studies. *AJNR Am J Neuroradiol* 1989; 10:777-786.
 8. Widius DM, Lammert GK, Brant A, et al. In vivo evaluation of isophendylate-cyanoacrylate mixtures. *Radiology* 1992; 185:269-273.
 9. Kailasnath P, Chaloupka JC. Quantitative assessment of polymerization-binding mechanics of cyanoacrylates: model development and validation. *AJNR Am J Neuroradiol* 2002; 23:772-786.

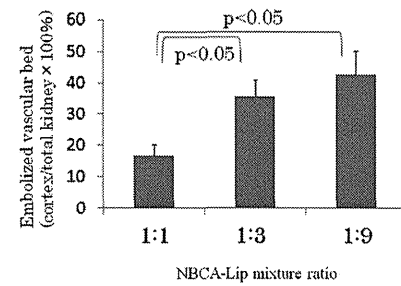


Figure E1. The embolized cortical vascular bed was increased as the Lip volume increased. The vascular bed was significantly greater with NBCA/Lip ratios of 1:3 and 1:9 than with an NBCA/Lip ratio of 1:1, whereas no significant difference was observed between NBCA/Lip ratios of 1:3 and 1:9.

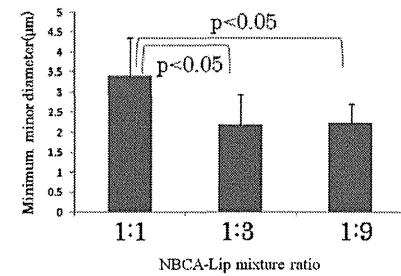


Figure E2. The minimum minor diameter of the arteriole containing embolic material in the lumen was measured in each kidney. With ratios of 1:3 and 1:9, the embolic material was found in significantly narrower arterioles than at a 1:1 ratio.

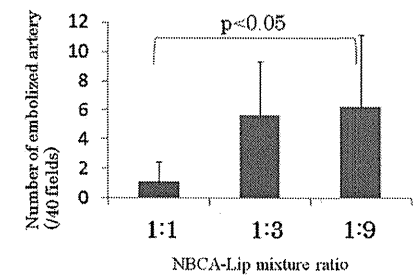


Figure E3. The number of arterioles with a minor diameter $\le 40 \mu m$ containing embolic material in the lumen was counted. At a low NBCA density, narrow arterioles were embolized, and the peripheral distribution of the embolic material tended to be broad. More arterioles were embolized at a 1:9 ratio than significantly at 1:1.

Reorientation of a Nonspherical Capsule in Creeping Shear Flow

Toshihiro Omori,^{1,*} Yohsuke Imai,² Takami Yamaguchi,¹ and Takuji Ishikawa,^{2,†}¹Department of Biomedical Engineering, Tohoku University, Aoba 6-6-01 Sendai Miyagi, Japan²Department of Bioengineering and Robotics, Tohoku University, Aoba 6-6-01 Sendai Miyagi, Japan
(Received 24 August 2011; published 28 March 2012)

The dynamics of a capsule and a biological cell is of great interest in chemical engineering and bioengineering. Although the dynamics of a rigid spheroid is well understood by Jeffery's theory, that of a spheroidal capsule remains unclear. In this Letter, the motion of a spheroidal capsule or a red blood cell in creeping shear flow is investigated. The results show that the orientation of a nonspherical capsule is variant under time reversal, though that of a rigid spheroid is invariant. Surprisingly, the alignment of a nonspherical capsule over a long time duration shows a transition depending on the shear rate, which can be utilized for a particle-alignment technique. These findings form a fundamental basis of the suspension mechanics of capsules and biological cells.

DOI: 10.1103/PhysRevLett.108.138102

PACS numbers: 47.63.mf, 83.50.-v, 87.16.D-

About a century ago, Jeffery analytically derived the motion of a nonspherical object in creeping linear background flow [1]. Since then, Jeffery's theory has been used to describe the alignment of rods and ellipsoids, such as bacteria, platelets, etc. The theory states that the trajectory of a non-Brownian rigid ellipsoid in Stokes flow is invariant under time reversal and that reorientation over a long time duration does not occur under simple shear flow conditions. The time reversibility can be destroyed by introducing inertia effects [2] or viscoelastic properties of the surrounding fluid [3], because the motion is no longer independent of time in these cases. However, the effect of particle deformability on the time reversibility is not well clarified. This study investigates this question by using a capsule as a model deformable object.

A capsule is a liquid drop enclosed by a deformable membrane, which is of great interest in the chemical engineering, bioengineering, and food industries. Many capsules in realistic situations are not perfect spheres because of the inhomogeneity of the membrane properties or folding due to unbalanced osmotic pressure. If one places a nonspherical capsule in creeping shear flow, how does the orientation change relative to the flow field over a long time duration? Jeffery speculated that an ellipsoid may alter its orientation so that the viscous energy dissipation of the system becomes minimal [1]. However, this may not be true for a capsule with a large deformation. Although many former studies have examined the dynamics of a nonspherical capsule [4–8], none of them can answer this question.

In this Letter, the motion of a non-Brownian spheroidal capsule or a red blood cell (RBC) in creeping shear flow is investigated numerically. The results show that the orientation of a nonspherical capsule is variant under time reversal, although the orientation of a rigid ellipsoid is invariant. Surprisingly, the alignment of a nonspherical capsule over a long time duration shows a transition

depending on the shear rate. The transition cannot be explained by the minimum energy dissipation, as speculated by Jeffery; the full fluid and solid mechanics are necessary to understand this phenomenon. The obtained results can be utilized for particle-alignment techniques in engineering applications and shed light on the complex dynamics of capsules and biological cells.

A capsule is assumed to be filled with an incompressible Newtonian fluid of viscosity $\lambda\mu$ and freely suspended in another fluid with the same density but viscosity μ . When the thickness of the capsule wall is small compared to its size and radius of curvature, the membrane can be modeled as a 2D hyperelastic surface without bending rigidity. In this study, we use two kinds of constitutive laws for the membrane: the neo-Hookean (NH) law [9] and the Skalak (SK) law [10]. The NH law describes isotropic volume-incompressible rubberlike material properties, whereas the Skalak law expresses the area incompressibility of a biological membrane.

To calculate capsule deformation accurately, fluid-structure interactions between the motion of the internal and external fluids and that of the capsule membrane have to be solved precisely. We assume that the flow is Stokesian, i.e., inertia-free, and the flow field is solved by a boundary element method. A finite element method is employed to solve the membrane mechanics. The governing equations and numerical methods are the same as in Refs. [6, 11], and the details are explained in Ref. [12]. The reference shape of the capsule is assumed to be spheroid or biconcave, in the same manner as in Refs. [5, 6]. The aspect ratio between the principal axes of the spheroid is represented by α . A linear triangular mesh with 5120 elements is used to discretize the membrane. The validation of the numerical methods is presented in Ref. [12].

In a Cartesian reference frame with the capsule center as the origin, the undisturbed linear background flow \mathbf{v}^∞ can be described as $\mathbf{v}^\infty = (\mathbf{E} + \boldsymbol{\Omega}) \cdot \mathbf{x}$, where \mathbf{E} and $\boldsymbol{\Omega}$ are the

rate of strain and rotation tensors, respectively. In this study, we use two types of background flow: (a) a simple shear flow given by $E_{xy} = E_{yx} = \Omega_{yx} = -\Omega_{xy} = \frac{\dot{\gamma}}{2}$ (all the other components = 0), as shown in Fig. 1(a), and (b) an oscillatory planar elongational flow given by $E_{xy} = E_{yx} = \frac{\dot{\gamma}}{2} \cos \omega t$ (all the other components = 0), as shown in Fig. 1(b). Here, $\dot{\gamma}$ is the shear rate or the elongational rate, t is the time, and ω is the angular velocity of the flow, which is correlated to the oscillation period T as $T = 2\pi/\omega$. The capillary number Ca represents the ratio of the viscous force to the elastic force and is given by $Ca = \mu\ell\dot{\gamma}/G_x$, where G_x is the membrane shear modulus and ℓ is the radius of a sphere that has the same volume as the ellipsoid or the biconcave capsule.

We first investigate the motion of a spheroidal oblate capsule in simple shear flow and compare the results with those of a rigid spheroid. To examine the capsule orientation efficiently, we define the orientation vector \mathbf{e} as a unit vector extending from the center of gravity and pointing to material point P located at the revolution axis of the unstressed spheroidal capsule. θ is defined as the angle between \mathbf{e} and the z axis, as shown in Fig. 1(c). At time $t = 0$, the oblate capsule without prestress is placed at an initial angle θ_0 of $\pi/4$. The deformation at time $t > 0$ due to the background shear is calculated until the steady periodic motion is achieved.

The motions of an oblate capsule with $Ca = 0.3$ and 1.0 are shown in Fig. 2(a) and 2(b), respectively ($\alpha = 0.6$, $\lambda = 1$, and NH membrane). The time history of θ is also shown in Fig. 2(c) for 30 periods of rotation. The results of a rigid spheroidal with the same α [1] are also plotted in the figure for comparison. Because of the nonspherical reference shape of the capsule membrane, θ oscillates twice during one rotation. In addition to the short-time oscillation, θ tends to approach towards 0 or $\pi/2$, depending on Ca , over a long time duration. The reorientation of the capsules is also clear in observing Figs. 2(a) and 2(b), because the material point P , which is indicated as a blue dot in the figures, moves towards $z = 0$ when $Ca = 0.3$, whereas it moves towards the z axis when $Ca = 1.0$. We note that the final orientation is independent of the initial orientation; this was confirmed numerically by changing

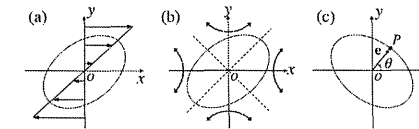


FIG. 1. Schematic illustration of a capsule in (a) simple shear flow and (b) oscillating planar elongational flow. (c) Orientation vector \mathbf{e} is defined as a unit vector extending from the center of gravity and pointing to material point P . θ is defined as the angle between \mathbf{e} and the z axis.

the initial orientation randomly. Such reorientation did not happen for a rigid spheroid, as shown in Fig. 2(c). These results clearly illustrate that a deformable capsule becomes reoriented, even in simple shear flow, and the time reversibility of Jeffery's orbit can be destroyed by introducing particle deformability.

The results of Fig. 2 raise another important question about why the reorientation direction shows a transition with increasing Ca . We calculated the viscous energy dissipation due to the capsule motion to determine whether the transition occurred to minimize the dissipation energy. However, we did not observe a one-to-one correlation between the capsule reorientation and the minimum energy dissipation. Thus, the full fluid and solid mechanics must be examined to answer this question.

To understand the basic mechanism of the transition, we further simplify the background flow field by deleting the rotational contribution from the shear flow. When an oblate capsule with an arbitrary initial orientation is subjected to steady planar elongational flow, the orientation is finally directed towards the compressing direction in all cases. Given that the reorientation transition does not appear in steady planar elongational flow, the steadiness in the flow field likely plays an important role in the transition.

Next, we apply oscillatory planar elongational flow, given by Fig. 1(b), to an oblate capsule. In this flow field, the elongational rate and changing frequency of the elongational direction can be independently controlled. At $t = 0$, the oblate capsule without prestress is placed at $\theta_0 = \pi/4$. The capsule motions for the second period of oscillation with $\omega/(\dot{\gamma}\pi) = 0.08$ and $Ca = 0.3$ and 1.0 are shown in Figs. 3(a) and 3(b) ($\alpha = 0.6$, $\lambda = 1$, and NH

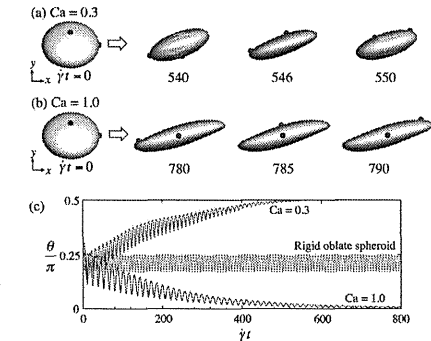


FIG. 2 (color). Oblate capsule in a simple shear flow with (a) $Ca = 0.3$ and (b) 1.0 ($\alpha = 0.6$, $\lambda = 1$, and NH membrane). Blue and red dots are material points on the membrane and are plotted as tracers. (c) Time change of θ , where the result of a rigid spheroid with same α [1] is also plotted for comparison.

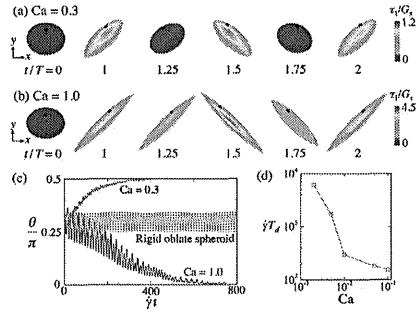


FIG. 3 (color). Motion of an oblate capsule in oscillating planar elongational flow with $\omega/(\dot{\gamma}\pi) = 0.08$ and (a) $Ca = 0.3$ or (b) $Ca = 1.0$ ($\alpha = 0.6$, $\lambda = 1$, and NH membrane). A black dot is placed at P as a tracer. (c) Time change of θ , where the result of a rigid spheroid with the same α [1] is plotted for comparison. (d) Dimensionless drift time in the small Ca regime.

membrane). Color contours show the distribution of τ_1 , where τ_i is the in-plane principal elastic tension and $\tau_1 \approx \tau_2$. The time history of θ is also shown in Fig. 3(c) for 20 periods of oscillation. When $Ca = 0.3$, θ approaches to $\pi/2$ after a sufficient time duration, whereas when $Ca = 1.0$, θ approaches to 0. For $Ca = 0.3$, the capsule deformation is small at $t/T = 1.25$ and 1.75 , when there is no background flow, and the τ_1 distributions at $t/T = 1.0$ and 1.5 are similar. For $Ca = 1.0$, however, large deformations remain at $t/T = 1.25$ and 1.75 , resulting in a strong asymmetry in the τ_1 distribution between $t/T = 1.0$ and 1.5 . Thus, the deformation is strongly affected by the time history in the high Ca regime, whereas it is quasisteady in the low Ca regime. This qualitative difference in the tension distribution likely causes the reorientation transition. When Ca is very small, the capsule should behave like a rigid body. In order to confirm the convergence, we calculate drift time T_d required for drifting from $\theta = \pi/4$ to $\pi/2$ and plot it in Fig. 3(d). We see that $\dot{\gamma}T_d$ increases rapidly as Ca is decreased, indicating convergence to the rigid body motion.

To clarify the reorientation phenomena in more detail, we plot a phase diagram of the final orientation as a function of Ca and $\omega/\dot{\gamma}\pi$. The oblate capsule is again subjected to the oscillatory planar elongational flow with $\theta_0 = \pi/4$. The computation is carried out for N periods of oscillation, and N is set to 30, as in Fig. 3(c). The convergence of the final angle is determined by the following equation: $|\theta_{30} - \theta_f| \leq \epsilon$, where θ_{30} is the average orientation vector of the 30th rotation, and $\theta_f = 0, \pi/2$, or θ_0 . The threshold value of $\epsilon = 0.05$ is used in this study, because the results with $\epsilon = 0.1$ and 0.05 are almost the

same. When the convergence criteria is not satisfied, we determined that the reorientation is in the transit regime.

The results of the phase diagram are shown in Fig. 4. The red region ($\theta_{30} \approx \theta_0$) indicates the rigid body motion or high frequency oscillation. When ω is very large, the capsule has little time to deform, which results in no obvious reorientation. When $Ca \rightarrow 0$, the capsular motion converges to the rigid body motion. Figure 3(d) indicates that the red region also appears in the $Ca < 0.001$ regime when $\omega/\dot{\gamma}\pi = 0.08$, though the diagram in this small Ca region is not plotted due to extremely high computational load. The green region ($\theta_{30} \approx \pi/2$) indicates the quasisteady deformation. This region appears when ω is small, including the steady planar elongation ($\omega = 0$). The magenta region indicates infinite stretching. This region appears only when the membrane is strain-softening, such as NH membrane. A strain-hardening membrane can avoid this problem [13]. The black region ($\theta_{30} \approx 0$) indicates large unsteady deformation. This region appears only when the capsule is subjected to the large elongation with the moderate oscillating frequency. The phase diagram may be slightly affected by the selection of N . Since N is limited in terms of the computational cost, we cannot technically increase $N \rightarrow \infty$. These results clearly illustrate that the convergence of $\theta \rightarrow 0$ appears only when the large deformation is affected by the time history.

In the case of shear flow, the elongational direction relative to the material point on the membrane oscillates with the angular velocity of the membrane motion. Thus, one may assume ω as the average rotational velocity of a capsule in shear flow and draw the curve shown in Fig. 4. The results of an oblate capsule in shear flow, shown in Fig. 2, are plotted in Fig. 4 by circles. A curve with small

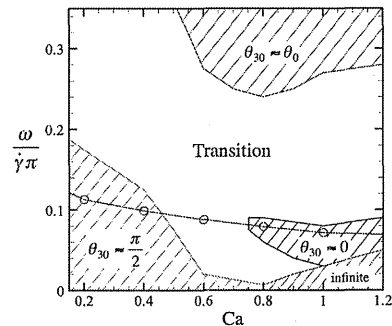


FIG. 4 (color). Phase diagram of the oblate capsule in oscillating elongational flow ($\alpha = 0.6$, $\lambda = 1$, and NH membrane). The circles in the figure indicate the converted results of the shear flow case.

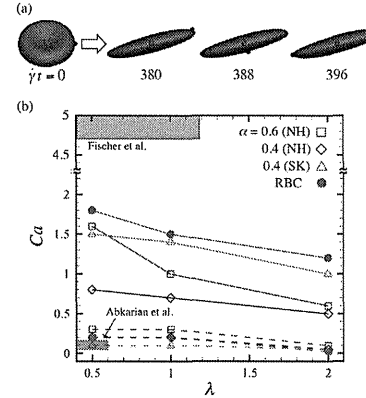


FIG. 5 (color). (a) Motion of a RBC in shear flow ($Ca = 2.0$, $\lambda = 1.0$). Blue and black dots are material points on the membrane and are plotted as tracers. (b) Effects of λ on the critical Ca number of oblate capsules and a RBC. The solid lines in the figure indicate Ca_0 , and the broken lines indicate $Ca_{\pi/2}$. Experimental conditions of Refs. [7,8] are plotted by gray and magenta regions, respectively.

Ca exists in the $\theta \rightarrow \pi/2$ region, whereas a curve with large Ca exists in the $\theta \rightarrow 0$ region. These results indicate that the reorientation transition found in the shear flow can also be explained by using Fig. 4.

Finally, we investigate the reorientation of a RBC in shear flow. The RBC membrane is modeled by the SK law with $C = 10$, where C is the ratio of area dilation to the shear modulus. Here we also investigate the effect of the viscosity ratio λ . Initially, the RBC is set to $\theta_0 = \pi/4$. The results of $Ca = 2$ and $\lambda = 1$ are shown in Fig. 5(a). Material point P , indicated as a blue dot in the figure, shifts to the z axis, i.e., $\theta \rightarrow 0$, for large Ca . When Ca was small, on the other hand, we confirmed that $\theta \rightarrow \pi/2$ in the same manner as the spheroidal capsule (data not shown). When $\theta = 0$, the RBC membrane has a pure tank-treading motion, and the membrane no longer oscillates during the rotation. When $\theta \neq 0$, on the other hand, the RBC shows a swinging motion, and the membrane oscillates during the rotation.

To effectively discuss the effect of λ and the constitutive law on the reorientation transition in shear flow, we define critical values of Ca : $Ca_{\pi/2}$ indicates the maximum Ca value to show $\theta_{30} \approx \pi/2$ convergence, and Ca_0 indicates the minimum Ca value to show $\theta_{30} \approx 0$ convergence. The results of a RBC as well as spheroidal capsules with $\alpha = 0.4$ and 0.6 and with two types of membrane constitutive laws are shown in Fig. 5 as a function of λ . $Ca_{\pi/2}$ and

Ca_0 tend to decrease as λ increased. This is because the time history of deformation remains for a longer time as the inside viscosity increased, which leads to the transition in the smaller Ca conditions. The figure also indicates that the effect of the constitutive law is considerable. A capsule with the SK membrane tends to have a larger critical Ca_0 than that with the NH membrane. This is because the SK law shows the strain-hardening property, whereas NH law shows the strain-softening, so large deformations are suppressed by the SK membrane. Thus, the reorientation transition can be understood by considering the fluid and solid mechanics of capsule deformation.

In Fig. 5, experimental conditions of Refs. [7,8] are plotted by gray and magenta regions, respectively, by assuming $\mu = 11\text{--}59 \text{ mPa} \cdot \text{s}$, $\dot{\gamma} = 800 \text{ s}^{-1}$ for Ref. [7] or $22\text{--}47 \text{ mPa} \cdot \text{s}$ and $\dot{\gamma} = 5 \text{ s}^{-1}$ for Ref. [8], and $G_v = 4 \text{ } \mu\text{N/m}$ and $\ell = 2.82 \text{ } \mu\text{m}$ for both cases. We see the experimental conditions of Ref. [7] are above Ca_0 , where our model shows the pure tank-treading motion as in Ref. [7]. The experimental conditions of Ref. [8] are below $Ca_{\pi/2}$, where our model shows the swinging motion as in Ref. [8]. Thus, the present results can nicely explain the difference of two former experimental observations by Refs. [7,8], even without introducing any inertial effect. We also note that the phase transition during reorientation is observed for a prolate spheroidal capsule, although the results are not included here. Thus, the reorientation transition is robust regardless of the reference shape of the capsule.

The results obtained in this study illustrate that the reorientation transition appears in a wide variety of artificial and biological capsules. Given that the transition can be controlled by adjusting the background flow strength as well as the unsteadiness in the background flow direction, the results obtained here can be utilized for particle-alignment techniques in engineering applications, such as counting nonspherical particles by light scattering, making anisotropic materials, etc. These findings form a fundamental basis for the suspension mechanics of capsules and biological cells.

We are grateful for helpful discussions with D. Barthès-Biesel and A.-V. Salsac of Université de Technologie de Compiègne.

*omori@pfsi.mech.tohoku.ac.jp
†ishikawa@pfsi.mech.tohoku.ac.jp

- [1] G. Jeffery, Proc. R. Soc. A 102, 161 (1922).
- [2] Z. Yu, N. Phan-Thien, and R. Turner, Phys. Rev. E 76, 026310 (2007).
- [3] Y. Iso, D. Koch, and C. Cohen, J. Non-Newtonian Fluid Mech. 62, 115 (1996).
- [4] P. Bagchi and R. Kalluri, Phys. Rev. E 80, 016307 (2009); D. Le and S. Wong, J. Comput. Phys. 230, 3538 (2011); S. Kessler, R. Finken, and U. Seifert, J. Fluid Mech. 605, 207

- (2008); P. M. Vlahovska, Y.-N. Young, G. Danker, and C. Misbah, *J. Fluid Mech.* **678**, 221 (2011); J. M. Skotheim and T. W. Secomb, *Phys. Rev. Lett.* **98**, 078301 (2007); Y. Sui, Y. T. Chew, P. Roy, X. B. Chen, and H. T. Low, *Phys. Rev. E* **75**, 066301 (2007).
- [5] S. Ramanujan and C. Pozrikidis, *J. Fluid Mech.* **361**, 117 (1998).
- [6] J. Walter, A.-V. Salsac, and D. Barthès-Biesel, *J. Fluid Mech.* **676**, 318 (2011).
- [7] T. Fischer, M. Stohr-Lissen, and H. Schmid-Schonbein, *Science* **202**, 894 (1978).
- [8] M. Abkarian, M. Faivre, and A. Viallat, *Phys. Rev. Lett.* **98**, 188302 (2007).
- [9] A. E. Green and J. E. Adkins, *Large Elastic Deformations* (Clarendon, Oxford, 1970), 2nd ed.
- [10] R. Skalak, A. Tozeren, R. P. Zarda, and S. Chien, *Biophys. J.* **13**, 245 (1973).
- [11] E. Foessel, J. Walter, A.-V. Salsac, and D. Barthès-Biesel, *J. Fluid Mech.* **672**, 477 (2011); T. Omori, T. Ishikawa, D. Barthès-Biesel, A.-V. Salsac, J. Walter, Y. Imai, and T. Yamaguchi, *Phys. Rev. E* **83**, 041918 (2011).
- [12] See Supplemental Material at <http://link.aps.org/supplemental/10.1103/PhysRevLett.108.138102> for movies.
- [13] W. R. Dodson III and P. Dimitrakopoulos, *Phys. Rev. Lett.* **101**, 208102 (2008).

Correspondence

High-Frame-Rate Echocardiography With Reduced Sidelobe Level

Hideyuki Hasegawa and Hiroshi Kanai

Abstract—Echocardiography has become an indispensable modality for diagnosis of the heart. It enables observation of the shape of the heart and estimation of global heart function based on B-mode and M-mode imaging. Methods for echocardiographic estimation of myocardial strain and strain rate have also been developed to evaluate regional heart function. Furthermore, it has been recently shown that echocardiographic measurements of transmural transition of myocardial contraction/relaxation and propagation of vibration caused by closure of the heart valve would be useful for evaluation of myocardial function and viscoelasticity. However, such measurements require a frame rate (typically >200 Hz) much higher than that achieved by conventional ultrasonic diagnostic equipment. We have recently realized a high frame rate of about 300 Hz with a full field of view of 90° using diverging transmit beams and parallel receive beamforming. Although high-frame-rate imaging was made possible by this method, the side lobe level was slightly larger than that of the conventional method. To reduce the side lobe level, phase coherence imaging has recently been developed. Using this method, the spatial resolution is improved and the side lobe level is also reduced. However, speckle-like echoes, for example, echoes from the inside of the heart wall, are also suppressed. In the present study, a method for reducing the side lobe level while preserving speckle-like echoes was developed. The side lobe level was evaluated using a wire phantom. The side lobe level of the high-frame-rate imaging using unfocused diverging beams was improved by 13.3 dB by the proposed method. In *in vivo* measurements, a B-mode image of the heart of a 23-year-old healthy male could be obtained while preserving the speckle pattern in the heart wall at a frame rate of 316 Hz with a full field of view of 90°.

I. INTRODUCTION

ECHOCARDIOGRAPHY is a predominant modality for diagnosis of the heart because it provides a cross-sectional image of the heart noninvasively in real time. Because of the high temporal resolution of ultrasonic diagnostic equipment, global heart function, such as ejection fraction (EF), can be estimated based on B-mode and M-mode imaging much more easily than with other diagnostic modalities, such as magnetic resonance imaging (MRI) and computed tomography (CT). It has recently been shown that ultrasonic measurements of transmural transition of myocardial contraction/relaxation and its propagation [1], [2] and propagation of vibration caused by closure of a heart valve would be useful for evaluation of myocardial function and viscoelasticity [3], [4]. How-

ever, such measurements require a frame rate much higher than that achieved by conventional ultrasonic diagnostic equipment. For example, electrical excitation propagates in Purkinje fibers and ventricular muscle at typical velocities of 0.3 to 4 m/s [5], and the corresponding propagation velocities of myocardial contraction of 0.5 to 7 m/s have been measured by ultrasound [4], [6]. In these studies, a high frame rate (typically higher than 400 Hz with a slightly reduced lateral field of view, which is much higher than that realized by conventional ultrasonic diagnostic equipment, usually several tens of hertz) is required to measure the propagation of this electromechanical wave and the resulting transient small motion of the heart wall.

Konofagou *et al.* [7] and D'hooge *et al.* [8] increased the frame rate to above 200 Hz in the ultrasonic measurement of the heart function. However, the size of the field of view and the total number of scan lines in an ultrasonic image were significantly reduced.

To achieve a high frame rate, we used sparse sector scanning, in which the number of scan lines was decreased to about 10 [9], and applied it to various applications [1]–[4]. In this method, the angle intervals between scan lines are increased to obtain a large lateral field of view with a small number of scan lines. Therefore, the lateral image resolution is significantly degraded.

The aforementioned methods are based on conventional beamforming; therefore, the density of scan lines or field of view must be sacrificed to achieve a high frame rate. To overcome this problem, parallel receive beamforming [10] with a wide transmit beam has been developed to illuminate a wider region by one transmission to reduce the number of transmissions. Lu and colleagues proposed an imaging method using an unfocused but nondiverging transmit beam, namely, a limited diffraction beam [11]–[14]. Unfocused beams achieved a wider beam width, and nondiverging beams used in these cited studies prevented the insonified energy from being spread to ensure that the required penetration depth was achieved. However, the width of a nondiverging beam is limited by the size of the aperture, which would limit the number of receiving beams created by one transmission.

High-frame-rate echocardiography at about 300 Hz with a full field of view of 90° using steered diverging transmit beams and parallel receive beamforming has recently been realized [15]. Diverging waves were produced using all transducer elements in an ultrasonic array probe to obtain ultrasonic echoes with a better SNR [16], [17] than the spherical wave produced by a single element [18]. Although just the idea of a diverging beam produced from multiple elements was shown in [17], the feasibility of the diverging beam had not been examined. The diverging beam from multiple elements was shown to be feasible in high-frame-rate echocardiography [15]. Although high-frame-rate imaging is possible by our method, the side lobe

level is slightly larger than that of conventional beamforming. To reduce the side lobe level, phase coherence imaging has recently been developed [19]. This method sensitively suppresses echoes influenced by the diversity of phases of echoes received by transducer elements because of various factors, such as focusing error, etc. Therefore, the spatial resolution is improved and the side lobe level is suppressed by this method, but weak speckle-like echoes, which are generated by interference of scattered echoes, are also significantly suppressed because the phases of echoes would be influenced by the interference. In the present study, a method to reduce the side lobe level while preserving speckle-like echoes was developed. The side lobe level was evaluated using a wire phantom, and a B-mode image of a heart of a 23-year-old healthy male was obtained *in vivo* by the proposed method.

II. PRINCIPLES

Using an unfocused wide transmit beam increases the side lobe level compared with conventional beamforming (focusing both in transmit and receive). Therefore, methods for reduction of the side lobe level are required.

When receive focusing is performed with respect to a spatial point p , the position of the source of an echo does not always exactly coincide with p . Let us consider the difference between the time delay applied by a receive beamformer and the propagation time delay of the echo. As shown in Fig. 1(a), the locations of focus and the source of the echo are defined by (x, z) and $(x + \Delta x, z + \Delta z)$, respectively. Under such conditions, distance r'_i from the i th element to the source and distance r_i from the i th element to the focal point are expressed as

$$r'_i = \sqrt{(x - x_i + \Delta x)^2 + (z + \Delta z)^2}, \quad (1)$$

$$r_i = \sqrt{(x - x_i)^2 + z^2}, \quad (2)$$

where x_i is the lateral position of the i th element.

Residual time delay $\Delta\tau_i$ (focusing error) of the echo from the source received by the i th element after receive beamforming (applying time delay $T_{\text{RBF},i}$) depends on the difference between r_i and r'_i .

$$\begin{aligned} (r'_i)^2 - r_i^2 &= \Delta\tau_i(2r_i + \Delta\tau_i) \\ &= (x - x_i + \Delta x)^2 + (z + \Delta z)^2 - (x - x_i)^2 - z^2, \end{aligned} \quad (3)$$

where $\Delta\tau_i$ is $r'_i - r_i$.

By assuming that the focal depth z is sufficiently large, squares of Δx and Δz can be neglected:

$$\Delta\tau_i(2r_i + \Delta\tau_i) \approx 2\Delta x(x - x_i) + 2\Delta z \cdot z, \quad (4)$$

$$\begin{aligned} \Delta\tau_i &= \frac{2\Delta x(x - x_i) + 2\Delta z \cdot z}{2r_i + \Delta\tau_i} \\ &\approx \frac{\Delta x(x - x_i) + \Delta z \cdot z}{r_i}, \end{aligned} \quad (5)$$

where $2r_i + \Delta\tau_i$ is approximated by $2r_i$ because $\Delta\tau_i$ is assumed to be sufficiently smaller than $2r_i$.

For large z , distance r_i can be approximated to be $(x^2 + z^2)^{1/2}$ because x_i is limited by the aperture size (x_i was less than 10 mm in the present study). Therefore, residual time delay $\Delta\tau_i$ is expressed as

$$\begin{aligned} \Delta\tau_i &= \frac{\Delta r_i}{c_0} \\ &\approx ax_i + b, \end{aligned} \quad (6)$$

where c_0 is the speed of sound. Constants a and b are given by

$$a = \frac{\Delta x}{c_0 \sqrt{x^2 + z^2}}, \quad (7)$$

$$b = \frac{\Delta x \cdot x + \Delta z \cdot z}{c_0 \sqrt{x^2 + z^2}}. \quad (8)$$

Residual time delay $\Delta\tau_i$ is also expressed as the residual phase delay $\Delta\theta_i$:

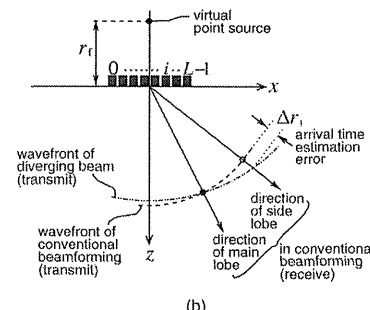
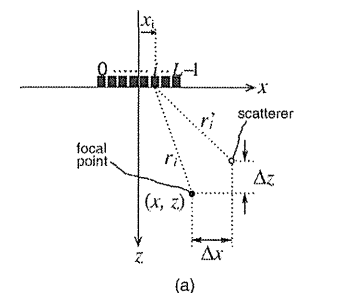


Fig. 1. Illustration of mismatch between the location of a focal point and that of the source of an echo (a) in receive and (b) in transmission.

Manuscript received December 20, 2011; accepted July 20, 2012.

The authors are with the Graduate School of Biomedical Engineering and the Graduate School of Engineering, Tohoku University, Sendai, Japan (e-mail: hasegawa@ecei.tohoku.ac.jp).

DOI: <http://dx.doi.org/10.1109/TUFFC.2012.2490>

$$\Delta\theta_i = 2\pi f_0 \Delta\tau_i \quad (9)$$

where f_0 is the center frequency of ultrasound. In the present study, a method was proposed for reduction of the side lobe level while keeping the shape of the point spread function similar to those in conventional beamforming and our proposed method using diverging beams. As shown in (6), there is a linear relationship between the residual phase delay $\Delta\theta_i$ and the lateral position x_i of an element when the location of a focal point is close to that of a scatterer. This means that the difference between residual phase delays of two neighboring elements is consistent across the array when the focusing is done near the source of an echo (when Δx and Δz are small). This consistency can be evaluated by the magnitude-squared coherence function (MSCF) γ [20], defined as:

$$\gamma = \frac{\left| \sum_{i=0}^{L-2} S_i^* \cdot S_{i+1} \right|^2}{\sum_{i=0}^{L-2} |S_i|^2 \sum_{i=0}^{L-2} |S_{i+1}|^2}, \quad (10)$$

where L is the number of elements. The numerator in (10) corresponds to the cross-spectrum between S_i and S_{i+1} averaged across the array. Therefore, the MSCF becomes 1 when the transfer function from S_i to S_{i+1} is constant across the array. On the other hand, the magnitude of the numerator decreases because of the incoherent averaging of the transfer function when the transfer function is not constant. The phase of the transfer function corresponds to the phase difference between two neighboring elements. Therefore, the MSCF would decrease when the phase difference between two neighboring elements is not constant [= nonlinear according to the element number (position)].

To obtain the MSCF γ , the complex Fourier coefficient S_i^* at f_0 ($= 3.75$ MHz) of the RF echo signal $s_i(t - T_{\text{RBF},i})$ received by the i th transducer element must be estimated. To obtain the complex Fourier coefficient S_i^* in the present study, the discrete Fourier transform at f_0 was applied to $s_i(t - T_{\text{RBF},i})$ with a Hann window whose length was $0.53 \mu\text{s}$. Under this condition, the first nulls of the power spectrum of the Hann window were located at 0 and 7.5 MHz, providing the available maximum bandwidth of the resultant complex signal S_i sampled at 30 MHz.

The Fourier transform was applied to the RF echo $s_i(t - T_{\text{RBF},i})$ received by the i th transducer element after the time shift by the receiving beamformer to account for the differences among propagation time delays of echoes received by transducer elements. However, the time delay $T_{\text{RBF},i}$ is an integral multiple of the sampling interval of the RF echo. To remove the residual time delay resulting from the difference between the actual time delay $\Delta\tau_i$ and $T_{\text{RBF},i}$, S_i^* is multiplied by $\exp[2\pi f_0(\Delta\tau_i - T_{\text{RBF},i})]$ to obtain the corrected Fourier coefficient \tilde{S}_i in (10). Therefore, there are no phase differences among corrected Fourier coefficients $\{\tilde{S}_i\}$ when the location of the source of the echo exactly coincides with the focal point p [the relationship between residual time delay and an element's lateral position is linear, but both a and b in (6) are zero]. In this

case, the MSCF γ is 1. In addition, according to (6) and (9), there is a linear relationship between the phase delay $\Delta\theta_i = \angle S_i$ and the lateral position x_i of the transducer element when the focal point is located very near the source of the echoes (small Δx and Δz). In such cases, the MSCF γ is also close to 1 because the phase difference between the spectra of the signals received by i th and $(i+1)$ th elements is consistent across the array. On the other hand, the MSCF γ decreases when there is a mismatch between the locations of the source of an echo and the focal point. (e.g., echoes caused by side lobes) because the assumption of (4) is not applicable. Therefore, such undesirable echoes can be suppressed by weighting the beamformed RF signal at p using the MSCF γ .

Furthermore, the difference between transmit beams in conventional and proposed beamforming is considered to affect the side lobe reduction. In conventional beamforming, the geometrical center (center of the aperture) is same in both transmit and receive, as illustrated in Fig. 1(b). Therefore, the time required for the propagation of ultrasound from the aperture to a scatterer (in transmit) and that from the scatterer to the aperture (in receive) are same, and an echo from a scatterer, which is located at the range distance along the side lobe that is same as the range distance of the focal point, would contribute to the calculation of the MSCF at the spatial point $p = (x, z)$.

On the other hand, the time required for the propagation from the aperture to the scatterer and that from the scatterer to the aperture are different in our beamforming using diverging beams because the geometrical center of the transmit beam is the position of a virtual source of a diverging beam. The time required for the propagation of a diverging beam from the aperture to a scatterer can be estimated correctly when the scatterer is located at the focal point. However, there is an arrival-time estimation error $\Delta\tau_i$, which reduces the contribution of the echo from the scatterer to the calculation of the MSCF at the spatial point p (there is no echo signal in beamforming at p when $\Delta\tau_i$ is larger than the pulse duration of ultrasound) when the scatterer is not at the focal point. Such arrival-time estimation error would also reduce the coherence of the received signals.

III. EVALUATION OF SPATIAL RESOLUTION AND SIDELobe LEVEL USING A WIRE PHANTOM

In the present study, a commercial diagnostic ultrasonic system (α -10, Aloka, Tokyo, Japan) was used with a 3.75 -MHz phased array probe. The phased array was composed of $L = 96$ elements at intervals of 0.2 mm. The elevation focal distance was fixed to be 70 mm. This system was modified so that all of the 96 elements can be excited simultaneously and RF echoes received by $L = 96$ individual elements could be acquired at a sampling frequency of 30 MHz and a 16 -bit resolution for off-line processing (receive beamforming, compounding, etc.). In conventional beamforming, receive focusing was done with

respect to each discrete spatial point. The beamforming procedure in our high-frame-rate imaging is described in [15]. The Hann apodization was used for both conventional beamforming and our high-frame-rate imaging. In the beamforming procedure, a constant speed of sound of 1540 m/s was assumed.

In the basic experiment, fine nylon wires (diameter $\approx 100 \mu\text{m}$) placed in water were used for evaluation of the spatial resolution. Figs. 2(a)–2(d) show B-mode images of the wires obtained by conventional beamforming and parallel beamforming with diverging beams at $r_f = 100$ mm without weighting, with weighting by the MSCF, and with weighting by the phase coherence factor [19], respectively, where r_f is the distance between the front surface of the array and the virtual point source behind the array for producing a diverging beam. The dynamic ranges of Figs. 2(a)–2(d) are 60 dB. For diverging beams, distance r_f was set at 100 mm. In Fig. 2, there is not much difference between the B-mode image obtained by conventional beamforming [Fig. 2(a)] and those obtained using diverging beams with [Fig. 2(b)] and without [Fig. 2(c)] weighting by the MSCF. The B-mode image obtained using diverging beams with weighting by the phase coherence factor [Fig. 2(d)] shows a significantly improved spatial resolution compared with the other images. In Fig. 2(d), the phase coherence factor is obtained as $\max\{0, 1 - \sigma/\sigma_0\}$ [19], where σ is the standard deviation of phases of echoes received by individual elements and $\sigma_0 = \pi/3^{0.5}$. The standard deviation σ was evaluated after applying time delays by the receiving beamformer.

Fig. 3 shows the lateral profiles of the images [corresponding to point spread functions (PSF)] at the shallowest wire. The half-full-widths at half-maxima of the point spread functions shown in Fig. 3 are provided in Table I. From the data shown in Fig. 3, the average side lobe levels were evaluated in the lateral angular ranges, $-45^\circ < (\text{lateral angle}) < -15^\circ$ and $15^\circ < (\text{lateral angle}) < 45^\circ$. The side lobe level obtained using diverging beams increased by 8.5 dB compared with conventional beamforming. By weighting with the MSCF, the side lobe level in the high-frame-rate imaging using diverging beams was reduced by 13.3 dB. Weighting by the phase coherence factor showed the best spatial resolution and the lowest side lobe level in the phantom experiment.

IV. IN VIVO IMAGING OF A HUMAN HEART

Figs. 4(a)–4(d) show B-mode images of the heart of a 23-year-old healthy male obtained by conventional beamforming and parallel beamforming with diverging waves at $r_f = 100$ mm without weighting, with weighting by the MSCF, and with weighting by the phase coherence factor, respectively. Fig. 5 shows the intensity profiles along the scan lines indicated by the white lines in Fig. 4. Note that the position of the posterior wall in the measurement with conventional beamforming was slightly shallower than that in the measurement with diverging beams.

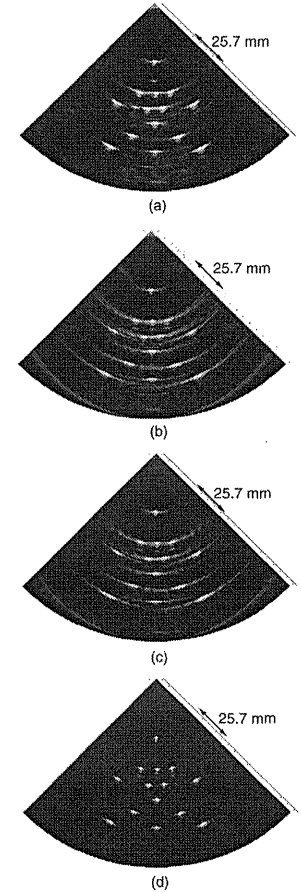


Fig. 2. B-mode images of fine wires obtained (a) by conventional sector scanning, (b) using a diverging beam, (c) using a diverging beam with weighting by the magnitude-squared coherence function (MSCF), and (d) using a diverging beam with phase coherence factor weighting [19].

Using diverging waves [Fig. 4(b)], a B-mode image of the heart could be obtained at a high frame rate of 316 Hz with a full lateral field of view of 90° . By weighting with the MSCF [Fig. 4(c)], the image contrast was improved, and speckle-like echoes, for example, echoes in the heart wall, were well preserved. It can be also observed in Fig. 5 that the proposed method using the MSCF suppresses the undesirable echoes in the cardiac lumen while keep-

TABLE I. HALF-FULL-WIDTHS AT HALF-MAXIMA OF POINT SPREAD FUNCTIONS SHOWN IN FIG. 3.

	Conventional beamforming	Diverging	Diverging with MSCF	Diverging phase coherence
Width of lateral PSF [mm]	0.66	0.82	0.81	0.43

ing the echoes inside the heart walls. On the other hand, by weighting with the phase coherence factor [Fig. 4(d)], speckle-like echoes inside the heart walls were significantly suppressed, although echoes resulting from specular reflection, such as an echo from the epicardium, were significantly enhanced. As shown in Fig. 3, although the spatial resolution is significantly improved by weighting with the phase coherence factor, this characteristic, i.e., significant suppression of speckle-like echoes, may not be preferable for analyzing the heart wall, such as estimation of velocity and strain rate of the heart wall.

V. DISCUSSION

Recently, we have developed a method based on parallel beamforming with diverging transmit beams for high-frame-rate echocardiography. To realize B-mode imaging in a sector format based on parallel beamforming, spherically diverging waves were used in transmission. However, in this method, the side lobe level slightly increased compared with that of conventional beamforming because of the use of unfocused transmit beams. In the present study, a method for reduction of side lobe level was developed to realize a side lobe level lower than that of conventional

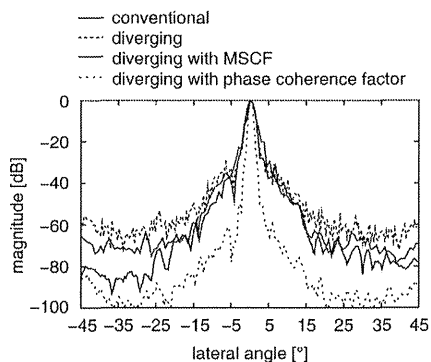


Fig. 3. Point spread functions in the lateral direction obtained by conventional sector scanning, diverging beam, diverging beam with weighting by the magnitude-squared coherence function (MSCF), and diverging beam with phase coherence factor weighting [19].

beamforming with a frame rate of over 300 Hz, which is much higher than that of conventional beamforming.

To consider small residual time delays of echoes, the phases of the echoes were used in the present study. To obtain the phase information, the Hilbert transform is used in general. However, the Hilbert transform requires the Fourier transform of the echo signal and the inverse Fourier transform of the estimated frequency spectrum. To increase the computational efficiency, in the present study, the Fourier coefficient of the echo at only the center frequency of ultrasound was calculated. This center frequency should be the center frequency of the received RF echo. However, in the present study, the center frequency of the ultrasound emitted was used because the estimation of the center frequency of the received echo required an additional computation. Before calculating the MSCF, time delays based on conventional focusing were applied to signals received by individual elements. In this procedure, sub-sample time delays were applied by considering the phase of the echo signal, as described in Section II. As expressed in (9), the phase delay coinciding with the corresponding time delay is expressed using the center frequency of the received echo. Therefore, there would be errors in application of time delays. However, such errors are negligible because the errors are smaller than the sampling interval of 25 ns.

In the results of imaging of wires, it was found that the side lobe reduction by the proposed method was depth-dependent, i.e., the side lobe reduction is smaller in a deeper region than a shallower region, because the change in the distance from a scatterer to an element caused by the lateral position of the element is smaller in a deeper region. As suggested for the phase coherence factor [19], the side lobe reduction can be controlled by taking γ^α (γ : MSCF), where α is a variable coefficient. Therefore, in our future work, it may be effective to control the weights by considering the depth-dependent characteristic of the MSCF γ .

To suppress the side lobe level, the phase coherence factor [19] was recently introduced. This method suppresses a beamformed echo signal whose standard deviation of phases of echoes received by transducer elements is large. Using this method, weak speckle-like echoes are also suppressed because the standard deviation of phases of echoes received by individual elements would be increased by interference of echoes, which is the source of speckle-like echoes. In some cases, it is important to observe speckle patterns of tissues. Therefore, a method for reduction of the side lobe level with preservation of speckle-like echoes was developed in the present study. On the other hand, the phase coherence factor improves spatial resolution and

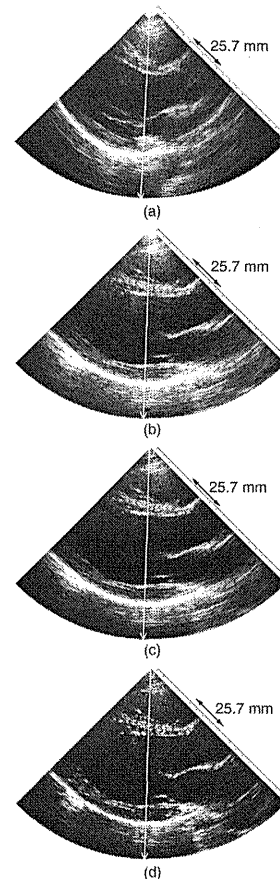


Fig. 4. B-mode images of the heart of a 23-year-old healthy male obtained (a) by conventional sector scanning, (b) using a diverging beam, (c) using a diverging beam with weighting by the magnitude-squared coherence function (MSCF), and (d) using a diverging beam with phase coherence factor weighting [19].

also well emphasizes specular echoes, such as echoes from heart valves in Fig. 4(d), and relatively strong scattering echoes. The method based on the phase coherence factor and the proposed method are complementary.

In high-frame-rate imaging, it is necessary to use unfocused transmit beams. Therefore, the side lobe level increases in general. Although optimization of transmit conditions, such as angular beam width, angular intervals

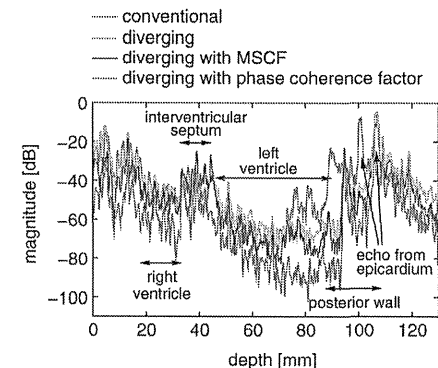


Fig. 5. Intensity profiles along the scan lines indicated by the white lines in Fig. 4.

of transmit beams, estimation of wavefronts of transmit beams, etc., are necessary to further improve the frame rate, such methods for reducing the side lobe level would be necessary for high-frame-rate imaging to obtain an image contrast comparable to or better than that obtained by conventional beamforming.

VI. CONCLUSIONS

In this study, a method of suppressing the side lobe level was developed for high-frame-rate echocardiography based on parallel beamforming with diverging transmit beams. To realize suppression of the side lobe level while preserving speckle-like echoes, the MSCF between echoes received by individual transducer elements was used for weighting a beamformed RF echo. Using the proposed method, it was confirmed by basic experiments using fine wires that the side lobe level could be reduced by 4.8 dB compared with conventional beamforming. Furthermore, in *in vivo* measurements, an ultrasonic image of a heart with a full field of view of 90° at a frame rate of 316 Hz could be obtained with an improved image contrast and preservation of speckle-like echoes.

REFERENCES

- [1] H. Kanai, "Propagation of vibration caused by electrical excitation in the normal human heart," *Ultrasound Med. Biol.*, vol. 35, no. 6, pp. 936–948, 2009.
- [2] H. Kanai and M. Tanaka, "Minute mechanical-excitation wave-front propagation in human myocardial tissue," *Jpn. J. Appl. Phys.*, vol. 50, no. 7, art. no. 07HA01, 2011.
- [3] H. Yoshizawa, H. Hasegawa, H. Kanai, and M. Tanaka, "Ultrasonic imaging of propagation of contraction and relaxation in the heart walls at high temporal resolution," *Jpn. J. Appl. Phys.*, vol. 46, no. 7B, pp. 4889–4896, 2007.

- [4] H. Kanai, "Propagation of spontaneously actuated pulsive vibration in human heart wall and *in vivo* viscoelasticity estimation," *IEEE Trans. Ultrason. Ferroelectr. Freq. Control*, vol. 52, no. 11, pp. 1931–1942, 2005.
- [5] D. M. Bers, *Excitation-Contraction Coupling and Cardiac Contractile Force*, 2nd ed., Dordrecht, The Netherlands: Kluwer Academic, 2001.
- [6] E. Konofagou, J. Luo, K. Fujikura, D. Cervantes, and J. Coronilas, "Imaging the electromechanical wave imaging of cardiovascular tissue *in vivo*," in *Proc. IEEE Ultrasonics Symp.*, 2006, pp. 985–988.
- [7] E. E. Konofagou, J. D'hooge, and J. Ophir, "Myocardial elastography—A feasibility study *in vivo*," *Ultrasound Med. Biol.*, vol. 28, no. 4, pp. 475–482, 2002.
- [8] J. D'hooge, E. Konofagou, F. Jamal, A. Heindal, L. Barrios, B. Bijnen, J. Thoen, F. van de Werf, G. Sutherland, and P. Suetens, "Two-dimensional ultrasonic strain rate measurement of the human heart *in vivo*," *IEEE Trans. Ultrason. Ferroelectr. Freq. Control*, vol. 49, no. 2, pp. 281–286, 2002.
- [9] H. Kansi and Y. Koiwa, "Myocardial rapid velocity distribution," *Ultrasound Med. Biol.*, vol. 27, no. 4, pp. 481–498, 2001.
- [10] D. P. Shattuck, M. D. Weinsztein, S. W. Smith, and O. T. v. Ramm, "Explososcan: A parallel processing technique for high speed ultrasound imaging with linear phased arrays," *J. Acoust. Soc. Am.*, vol. 75, no. 4, pp. 1273–1282, 1984.
- [11] J. Lu, "2D and 3D high frame rate imaging with limited diffraction beams," *IEEE Trans. Ultrason. Ferroelectr. Freq. Control*, vol. 44, no. 4, pp. 839–856, 1997.
- [12] J. Lu, "Experimental study of high frame rate imaging with limited diffraction beams," *IEEE Trans. Ultrason. Ferroelectr. Freq. Control*, vol. 45, no. 1, pp. 84–97, 1998.
- [13] J. Cheng and J. Lu, "Extended high-frame rate imaging method with limited-diffraction beams," *IEEE Trans. Ultrason. Ferroelectr. Freq. Control*, vol. 53, no. 5, pp. 880–890, 2006.
- [14] J. Lu, J. Cheng, and J. Wang, "High frame rate imaging system for limited diffraction array beam imaging with square-wave aperture weightings," *IEEE Trans. Ultrason. Ferroelectr. Freq. Control*, vol. 53, no. 10, pp. 1796–1812, 2006.
- [15] H. Hasegawa and H. Kanai, "High-frame-rate echocardiography using diverging transmit beams and parallel receive beamforming," *J. Med. Ultrasound*, vol. 38, no. 3, pp. 129–140, 2011.
- [16] M. O'Donnell and L. J. Thomas, "Efficient synthetic aperture imaging from a circular aperture with possible application to catheter-based imaging," *IEEE Trans. Ultrason. Ferroelectr. Freq. Control*, vol. 39, no. 3, pp. 366–380, 1992. http://www.ncbi.nlm.nih.gov/entrez/query.fcgi?cmd=Retrieve&db=PubMed&list_uids=18267646&dopt=Abstract
- [17] M. Karaman and M. O'Donnell, "Synthetic aperture imaging for small scale systems," *IEEE Trans. Ultrason. Ferroelectr. Freq. Control*, vol. 42, no. 3, pp. 429–432, 1995.
- [18] F. Gran and J. A. Jensen, "Directional velocity estimation using a spatio-temporal encoding technique based on frequency division for synthetic transmit aperture ultrasound," *IEEE Trans. Ultrason. Ferroelectr. Freq. Control*, vol. 53, no. 7, pp. 1289–1299, 2006.
- [19] J. Camacho, M. Parrilla, and C. Fritsch, "Phase coherence imaging," *IEEE Trans. Ultrason. Ferroelectr. Freq. Control*, vol. 56, no. 5, pp. 958–974, 2009.
- [20] G. C. Carter, C. H. Knapp, and A. H. Nuttall, "Estimation of the magnitude-squared coherence function via overlapped fast Fourier transform processing," *IEEE Trans. Audio Electroacoust.*, vol. AU-21, no. 4, pp. 337–344, 1983.